Role of Na$_v$1.6-mediated persistent sodium current and bursting-pacemaker properties in breathing rhythm generation

Carlos A. da Silva Jr.[1], **Cameron J. Grover**[1], **Maria Cristina D. Picardo**[1], **Christopher A. Del Negro**[1,2,*]

[1]Department of Applied Science, William & Mary, Williamsburg, VA 23185, USA

[2]Lead contact

SUMMARY

Inspiration is the inexorable active phase of breathing. The brainstem preBötzinger complex (preBötC) gives rise to inspiratory neural rhythm, but its underlying cellular and ionic bases remain unclear. The long-standing "pacemaker hypothesis" posits that the persistent Na$^+$ current (I_{NaP}) that gives rise to bursting-pacemaker properties in preBötC interneurons is essential for rhythmogenesis. We tested the pacemaker hypothesis by conditionally knocking out and knocking down the *Scn8a* (Na$_v$1.6 [voltage-gated sodium channel 1.6]) gene in core rhythmogenic preBötC neurons. Deleting *Scn8a* substantially decreases the I_{NaP} and abolishes bursting-pacemaker activity, which slows inspiratory rhythm *in vitro* and negatively impacts the postnatal development of ventilation. Diminishing *Scn8a* via genetic interference has no impact on breathing in adult mice. We argue that the *Scn8a*-mediated I_{NaP} is not obligatory but that it influences the development and rhythmic function of the preBötC. The ubiquity of the I_{NaP} in respiratory brainstem interneurons could underlie breathing-related behaviors such as neonatal phonation or rhythmogenesis in different physiological conditions.

In brief

da Silva Junior et al. show that conditional deletion of *Scn8a* (Na$_v$1.6) to reduce the persistent sodium current (I_{NaP}) in core breathing rhythmogenic neurons diminishes their excitability and impacts respiratory development without stopping breathing. Conditional *Scn8a* knockdown in mature mice does not affect breathing. These results advocate network-based breathing rhythmogenic mechanisms.

Graphical Abstract

INTRODUCTION

Breathing consists of rhythmic movements that ventilate the lungs initiated by a central pattern generator network in the brainstem. Inspiration is the inexorable active phase and emanates from the pre-Bötzinger complex (preBötC), a specialized site in the ventrolateral medulla.[1–4] Its core rhythmogenic interneurons are glutamatergic,[5,6] derived from precursor cells expressing the transcription factor *Developing Brain Homeobox 1* (*Dbx1*).[7–9]

Coincident with discovery of the preBötC, a subset of interneurons expressing voltage-dependent bursting properties[4] was hypothesized to constitute its oscillatory kernel, thus forming the "pacemaker hypothesis" of rhythmogenesis.[10] Cellular bursting-pacemaker properties depend principally on the persistent Na$^+$ current (I_{NaP}) being expressed at sufficient magnitude in concert with a relatively low-magnitude leakage K$^+$ current ($I_{K\text{-leak}}$). Thus, even though the I_{NaP} is expressed ubiquitously in the preBötC, only 5%–15% of its constituent neurons with the requisite ratio of I_{NaP} to $I_{K\text{-leak}}$ exhibit bursting-pacemaker activity.[4,11–18]

Whether the I_{NaP} and bursting-pacemaker properties contribute to inspiratory rhythmogenesis has not been resolved. Several attempts used Na$^+$ channel antagonists like riluzole and tetrodotoxin (TTX) to block the I_{NaP} but yielded incongruent results followed by incompatible interpretations. Riluzole and TTX applied in a neonatal rat slice model of breathing decelerated and then stopped the inspiratory rhythm, which supports the idea

that the I_{NaP} and bursting-pacemaker properties are obligatory for rhythmogenesis.[12] Similar experiments in neonatal mouse slices showed that rhythm cessation was irreversible.[19] Riluzole applied in rhythmic mouse embryo slices at embryonic day 16.5 (E16.5) stopped inspiratory rhythmic activity, although the same treatment at E18.5 failed to stop it, from which the authors conclude that the I_{NaP} and bursting-pacemaker properties are relevant for embryonic preBötC function but ultimately non-essential.[20] Different groups working with neonatal mouse slices found that riluzole and TTX abolished the voltage-dependent bursting-pacemaker behavior in preBötC neurons, as expected, but that those drugs did not affect the inspiratory frequency,[14,18,21] indicating that the I_{NaP} and bursting-pacemaker activity are superfluous for rhythmogenesis.

Those contradictory reports leave unsolved the cellular bases of inspiratory rhythmogenesis. Here, we identify the flaws of past studies and adopt a new approach to avoid them. The confounding issues of past studies are attributable to pharmacological blockers with promiscuous and non-selective effects. Riluzole depresses excitatory transmission via inhibiting glutamate release as well as postsynaptic receptor activity,[22–24] which could be the actual cause of riluzole-induced rhythm cessation in some experiments rather than attenuation of the I_{NaP}. In the experiments where riluzole did not stop the rhythm, a modeling study argues that the I_{NaP} can escape riluzole blockade by being reactivated via transient hyperpolarizing perturbations from inhibitory neurons in the interval between inspiratory bursts, ruling out any interpretation of those experiments from the standpoint of blocking the I_{NaP}.[25]

In addition to the inconclusive pharmacological studies *in vitro*, we still lack categorical experiments *in vivo* that can interrogate the role of the I_{NaP}, and thus bursting-pacemaker properties, in awake animals from neonatal to adult stages of development. Thus, new approaches, using genetic tools to selectively target the I_{NaP} in the core rhythmogenic population and avoid off-target effects, are required to elucidate the role, or lack thereof, of this ionic mechanism in rhythmogenesis.

The I_{NaP} is a feature of the voltage-gated sodium channel 1.6 (Na$_v$1.6), encoded by the *Scn8a* gene.[26–32] Deletion of *Scn8a* causes a 70%–76% reduction in the I_{NaP} in null mice.[28,31] Therefore, although Na$_V$1.1, Na$_V$1.2, Na$_V$1.3, Na$_V$1.6, and Na$_V$1.9 are expressed in rhythmogenic preBötC neurons,[15,33–35] Na$_V$1.6 (*Scn8a*) is the most promising candidate target for genetic manipulation to evaluate the role of the I_{NaP} and of bursting-pacemaker properties in rhythmogenesis.

Therefore, we attenuated *Scn8a* (Na$_v$1.6) expression in core inspiratory rhythmogenic preBötC neurons via short hairpin RNA (shRNA) silencing technology (conditional knockdown) and precluded *Scn8a* expression in *Dbx1*-derived neurons (here-after: Dbx1 neurons), including those in preBötC, using intersectional mouse genetics (conditional knockout). We predict that if the I_{NaP} and bursting-pacemaker properties underlie or significantly contribute to inspiratory rhythmogenesis, then *Scn8a* diminution should decelerate, stop, or otherwise perturb breathing in awake intact neonatal and adult mice, as well as in rhythmically active slice preparations.

RESULTS

Conditional *Scn8a* knockout reduces I_{NaP} in glutamatergic preBötC neurons

We performed whole-cell patch-clamp recordings from *VGlut2*-expressing preBötC neurons in VGlut2;Ai9;Scn8a mice, which reflects the intersection of a VGlut2-ires-cre driver strain and two Cre-responder strains: a tdTomato reporter (Ai9) for cell identification (Figure 1A) as well as a strain where the first exon of *Scn8a* is flanked by *loxP* sites, allowing for conditional gene deletion.[36]

We isolated Na^+ currents using a patch pipette solution containing Cs^+ as well as a bathing solution containing tetraethylammonium (TEA) and Cd^{2+}. *VGlut2;Ai9;Scn8a^{+/+}* wild-type mice (Figure 1B, left) showed a quasi-steady-state current-voltage (I-V) curve (black line) whose region of negative slope resistance initiated at approximately –57 mV, the base of the I_{NaP} activation curve.[12,13] The I-V curve from *VGlut2;Ai9;Scn8a^{fl/fl}* mice showed a region of negative slope resistance that initiated at approximately –57 mV but with much less peak inward current (Figure 1B, right, black line). TTX blocked the region of negative slope resistance completely as expected for the I_{NaP} (Figure 1B, gray lines). The I_{NaP} measured 2.30 ± 0.50 pA pF^{-1} in *VGlut2;Ai9;Scn8a^{+/+}* mice (N = 3), 1.37 ± 0.43 pA pF^{-1} in *VGlut2;Ai9;Scn8a^{fl/+}* mice (N = 2, a 40.5% reduction), and 0.79 ± 0.23 pA pF^{-1} in *VGlut2;Ai9;Scn8a^{fl/fl}* mice (N = 3, a 65.6% reduction). Linear regression analysis returned a slope of –0.16 pA pF^{-1} per deleted *Scn8a* allele, which is significantly non-zero ($r^2 = 0.78$, $p = 0.003$) (Figure 1C). The coefficient of determination (r^2) demonstrates that 78% of the diminution of the I_{NaP} is attributable to loss of *Scn8a*.

Next, we examined how 40.5% and 65.6% reductions in the I_{NaP} would affect the behavior of preBötC bursting-pacemaker neurons according to the canonical mathematical model[11] (Figure 1D). With persistent Na^+ conductance (g_{NaP}) at its standard value of 2.8 nS, the model neuron exhibits silent, bursting, and tonic spiking states depending on excitability governed by the reversal potential of I_{K-leak} (E_L). However, reducing the conductance by either 40.5% or 65.6% prevents bursting-pacemaker activity regardless of E_L; only silent and tonic spiking states are then possible. These simulations suggest that bursting-pacemaker behavior would not be possible in glutamatergic preBötC neurons following I_{NaP} reductions in *VGlut2;Ai9;Scn8a^{fl/+}* and *VGlut2;Ai9;Scn8a^{fl/fl}* mice.

Conditional *Scn8a* knockout precludes bursting-pacemaker activity in glutamatergic preBötC neurons but inspiratory rhythmogenesis perdures at lower frequency

We used multiphoton imaging to measure cytosolic Ca^{2+} in glutamatergic preBötC neurons in rhythmic slices from VGlut2;Ai148;Scn8a mice (Figure 2). This mouse reflects the intersection of the VGlut2-ires-cre driver strain and two Cre-responder strains: the first (Ai148) features the genetically encoded Ca^{2+} indicator GCaMP6f, and the second is the *Scn8a* conditional knockout strain.

We recorded the activity of multiple neurons simultaneously in *VGlut2;Ai148;Scn8a^{+/+}* slices (wild type) and in *VGlut2; Ai148;Scn8a^{fl/+}* slices (heterozygous) while monitoring inspiratory-related motor output from the hypoglossal (XII) cranial nerve. Conditional full knockout *VGlut2;Ai148;Scn8a^{fl/fl}* pups were not viable. In control conditions, rhythmically

active glutamatergic neurons discharged in sync with XII output in wild-type (Figure 2A, top panel) and heterozygous (Figure 2A, bottom panel) mouse slices. The frequency in *VGlut2;Ai148;Scn8a*$^{+/+}$ slices measured 0.17 ± 0.034 Hz (n = 114 neurons in N = 5 slices), whereas the frequency in *VGlut2;Ai148;Scn8a*$^{fl/+}$ slices measured 0.12 ± 0.049 Hz (n = 98 neurons in N = 5 slices), which was significantly different ($p = 1 \times 10^{-14}$) (Figure 2B). These data show that slices from both genotypes produce inspiratory rhythm but that loss of one allele of *Scn8a* in glutamatergic neu rons depresses the baseline frequency of the inspiratory rhythm by ~0.05 Hz.

Next, we imaged the same neurons after adding a cocktail of ionotropic synaptic receptor antagonists. Stopping ionotropic receptor-mediated synaptic transmission in *VGlut2;Scn8a*$^{+/+}$ slices silenced the XII nerve output and a large fraction of the glutamatergic preBötC neurons. Nevertheless, 12 different glutamatergic neurons from 5 different slices (11% of 114 neurons imaged) continued to generate rhythmic fluorescence transients at frequencies ranging from 0.05 to 0.15 Hz (Figures 2A and 2B). Rhythmic changes in fluorescence at these frequencies, following blockade of synaptic activity, is the signature of cellular bursting-pacemaker activity in the preBötC.[37] In contrast, no neuron remained rhythmically active in *VGlut2;Ai148;Scn8a*$^{fl/+}$ slices in the presence of the cocktail of synaptic blockers (Figures 2A and 2B), indicating a lack of bursting-pacemaker behavior in glutamatergic neurons following a single *Scn8a* allele deletion. Next, 1 μM TTX application stopped rhythmic activity of the subset of bursting neurons in *VGlut2;Ai148;Scn8a*$^{+/+}$ slices, which indicates that their bursting-pacemaker activity depended on the I_{NaP} (Figures 2A and 2B).

Breathing continues with impairments, and locomotion is ataxic in Dbx1;Scn8a conditional knockout mice *Molecular assays*

We examined breathing in Dbx1;Scn8a mice, which reflects the intersection of a *Dbx1*^{Cre} driver strain[38] with the *Scn8a* conditional knockout strain, in which offspring lack *Scn8a* expression in *Dbx1*-derived neurons. We chose to use the *Dbx1*^{Cre} driver because it affects a smaller subset of neurons throughout the nervous system compared with the VGlut2-ires-cre strain, yet the *Dbx1*^{Cre} driver strain will cause *loxP* recombination in interneurons that comprise the rhythmogenic preBötC core, wherein *Dbx1* and *VGlut2* demarcate the same preBötC neurons.[7,8] Genotype was confirmed via PCR post hoc (Figure S1). We assessed *Scn8a* expression via multiplex *in situ* hybridization at the end of the ventilatory measurements in *Dbx1;Scn8a*$^{+/+}$, *Dbx1;Scn8a*$^{fl/+}$, and *Dbx1;Scn8a*$^{fl/fl}$ mice (Figures 3A and S2). Core preBötC neurons were identified via transcription factor *Even-Skipped Homeobox 1* (*Evx1*), which is expressed postmitotically in *Dbx1*-derived neurons.[33,39] We observed *Scn8a* co-expression with *Evx1* in sections obtained from *Dbx1;Scn8a*$^{+/+}$ and *Dbx1;Scn8a*$^{fl/+}$ mice, whereas no *Scn8a* was detectable in *Evx1*-expressing neurons in sections from *Dbx1;Scn8a*$^{fl/fl}$ mice (Figures 3A and S2). We did not quantify the difference in expression between *Dbx1;Scn8a*$^{+/+}$ and *Dbx1;Scn8a*$^{fl/+}$ mouse sections because patch-clamp recordings (Figure 1C) provided a direct measure of I_{NaP} diminution following *Scn8a* deletion in core preBötC neurons.

Respiratory variables—We measured ventilation $(\dot{V}_E)$, tidal volume (V_T), respiratory frequency (f_R), and the air convection requirement $(\dot{V}_E/\dot{V}_{O_2})$ in Dbx1;Scn8a mice from postnatal day 0 (P0) up to early adulthood (P21) (Figure S3). Figures 3B–3E and S4A and Table 1 present the linear regression analyses for the respiratory measurements in each group. $\dot{V}_E$ increased with age in all the three groups (i.e., the slope of the regression line was significantly non-zero). The increase in $\dot{V}_E$ during postnatal development was due to an increase in V_T for each group because f_R did not change during the observation period. $\dot{V}_E/\dot{V}_{O_2}$ also increased during postnatal development in all groups of mice. Oxygen consumption $(\dot{V}_{O_2})$ decreased in *Dbx1;Scn8a$^{+/+}$* control mice but did not change during the postnatal observation period in *Dbx1;Scn8a$^{fl/+}$* and *Dbx1;Scn8a$^{fl/fl}$* mice (Figure S4A).

We assessed whether there was an effect of genotype, i.e., whether respiratory development differed between the groups, by comparing the slopes of the regression lines for each of the respiratory variables analyzed. We detected a significant effect of genotype on $\dot{V}_E$ ($p = 0.015$) and $\dot{V}_E/\dot{V}_{O_2}$ ($p = 0.0007$), suggesting that although $\dot{V}_E$ and $\dot{V}_E/\dot{V}_{O_2}$ increased in all three groups during development, *Dbx1;Scn8a$^{fl/fl}$* mice increased less than *Dbx1;Scn8a$^{fl/+}$* or *Dbx1;Scn8a$^{+/+}$* mice (Figures 3B and 3E).

We also detected a significant effect of genotype on f_R ($p = 0.037$), but the interpretation is not straightforward because none of the groups exhibited statistically significant change in f_R during development (the slope of each group's regression line was ostensibly zero). The groupwise difference in the regression lines is probably because *Dbx1;Scn8a$^{fl/+}$* mice presented a positive slope, whereas *Dbx1;Scn8a$^{fl/fl}$* and *Dbx1;Scn8a$^{+/+}$* mice had a negative slope, which results in statistically significant disparity between groups (Figure 3D). We detected no effect of genotype on V_T ($p = 0.25$; Figure 3C) or $\dot{V}_{O_2}$ ($p = 0.23$; Figure S4A).

The inspiratory time (T_I), expiratory time (T_E), and the inspiratory drive (V_T/T_I) were also measured and analyzed (Figures S4B–S4D; Table 1). We detected no changes in T_I during postnatal development for any of the groups and no significant effect of genotype ($p = 0.08$). T_E did not change during postnatal development in *Dbx1;Scn8a$^{+/+}$* mice. Paradoxically, T_E decreased in *Dbx1;Scn8a$^{fl/+}$* mice yet increased in *Dbx1;Scn8a$^{fl/fl}$* mice during postnatal development, resulting in a significant genotype effect ($p = 0.0004$). We do not consider these effects to be physiologically relevant because the changes in T_E were both on the order of 4–7 ms per day, which is relatively small compared with the typical ~350 ms breathing cycle. Lastly, V_T/T_I did not change during postnatal development in *Dbx1;Scn8a$^{+/+}$* mice, but it increased significantly in *Dbx1;Scn8a$^{fl/+}$* and *Dbx1;Scn8a$^{fl/fl}$* mice. These developmental disparities in V_T/T_I did not result in a significant effect of genotype ($p = 0.072$; Figure S4D), so it is not clear whether V_T/T_I disparities can be attributed to conditional *Scn8a* deletion.

Locomotion—*Dbx1;Scn8a$^{fl/fl}$* mice developed locomotor ataxia that became apparent after age P10. When placed in the prone position, *Dbx1;Scn8a$^{fl/fl}$* mice remained immobile with hindlimbs in hyperextension, often dragging their hyperextended hind legs in tandem rather than executing left-right alternating steps (Video S1). *Dbx1;Scn8a$^{fl/+}$* and

Dbx1;Scn8a$^{+/+}$ mice exhibited normal left-right alternation in stepping throughout postnatal development but with a wide stance (Video S2).

Survival analysis—Zero out of four *Dbx1;Scn8a$^{+/+}$* mice died, whereas two out of nine *Dbx1;Scn8a$^{fl/+}$* mice died and five out of eight *Dbx1;Scn8a$^{fl/fl}$* mice died, during postnatal development (Figure S5A). The hazard ratio for premature death was 2.81 for the homozygous *Dbx1;Scn8a$^{fl/fl}$* mice with respect to heterozygous *Dbx1;Scn8a$^{fl/+}$* mice. A hazard ratio cannot be computed with respect to *Dbx1;Scn8a$^{+/+}$* control mice because none died. We reject the null hypothesis that the survival curves of *Dbx1;Scn8a$^{fl/fl}$* and *Dbx1;Scn8a$^{fl/+}$* mice are identical based on a log-rank (Mantel-Cox) method of comparison (p = 0.04), which means that homozygous conditional knockout mice are more likely to die prematurely compared with mice from other groups.

Body mass—*Dbx1;Scn8a$^{+/+}$* and *Dbx1;Scn8a$^{fl/+}$* mice gained body mass during postnatal development at the rate expected for mice with a C57BL/6 background (which gain 0.5 g per day, RRID: IMSR_JAX:000664), attaining average body masses of 13.1 ± 0.7 g (*Dbx1;Scn8a$^{+/+}$*) and 11.6 ± 1.8 g (*Dbx1;Scn8a$^{fl/+}$*) at the end of the observation period (Figure S5B). Their body masses at the end of the observation period were well within the 95% confidence intervals for C57BL/6 mice published by the Jackson Lab oratory (Bar Harbor, ME, USA). *Dbx1;Scn8a$^{fl/fl}$* mice gained body mass too, reaching 6.03 ± 2.7 g by the end of the observation period (Figure S5B), but their rates of body mass gain and final body mass are outside the 95% confidence intervals for C57BL/6 mice. Therefore, there was a significant effect of genotype on gain of body mass during postnatal development (p = 1.2 × 10^{-6}).

These data and statistics suggest that single deletion of *Scn8a* from Dbx1 neurons has a negligible impact on breathing frequency and its development and maturation from birth to early adulthood. However, removal of both *Scn8a* alleles from Dbx1 neurons has a negative impact on development of $\dot{V}_E$ and air convection, and it results in a severe locomotor phenotype predominantly affecting the hindlimbs. The changes in $\dot{V}_E$ and locomotion appear to impede development including augmentation of body mass, and the resulting phenotype is often fatal.

Breathing is unimpaired after conditional knockdown of *Scn8a* in glutamatergic preBötC neurons

We performed virus microinjections in the preBötC of VGlut2-ires-cre adult mice (Figure S6A) to attenuate *Scn8a* expression in core rhythmogenic neurons. The adeno-associated virus (AAV) in the experimental group carried a Cre-dependent shRNA sequence targeting *Scn8a*. The AAV in the control group carried a non-targeting shRNA sequence consisting of the same nucleotides but in a scrambled order. Both viruses carried the Cre-dependent fluorescent tag mCherry for post hoc identification of the microinjection site and transduced neurons.

We detected mCherry-expressing neurons adjacent to well-established landmarks that colocalize with the preBötC such as the loop of the inferior olive (IO$_{loop}$), the semi-compact

division of the nucleus ambiguus (NA$_{sc}$), and the fourth ventricle near the obex (Figure S6B).[40,41] The mCherry expression was detected from bregma levels −6.8 to −7.1 mm, encompassing the anterior-posterior range of the preBötC. mCherry expression was densest near the ventral border of the brainstem where the preBötC is located, and it diminished dorsally in the reticular formation, which hosts output-related inspiratory neurons and dedicated inspiratory premotor neurons (Figure S6C).[12,42]

We measured *Scn8a* expression via multiplex *in situ* hybridization in glutamatergic preBötC neurons of mice injected with *Scn8a*-targeting and non-targeting shRNA (Figures 4A, 4B, and S7). Transcript counts, based on puncta that represent single transcript copies visible via RNAscope detection, differ visibly between control and *Scn8a*-targeting shRNA-injected mice. For example, in Figure 4A, the cyan arrow in the bottom panel shows *Scn8a* expression in a non-glutamatergic neuron from the experimental group that exceeds *Scn8a* expression of an adjacent virus-transduced glutamatergic neighbor and that is commensurate with *Scn8a* expression in the virus-transduced glutamatergic neuron from the control group shown in the top panel.

We quantified *Scn8a* expression using the same detection threshold across all sections and mice (Figures 4C and 4D). We excluded clusters of puncta from this analysis because the number of transcripts in a cluster is unknowable. Mice injected with *Scn8a*-targeting shRNA showed significantly lower *Scn8a* expression compared with control mice at 2 and 6 weeks following AAV injection (2 weeks: 15.9 ± 11.5 neuron^{-1} vs. 27.8 ± 7.6 neuron^{-1}, p = 4.7 3 10^{-5}; 6 weeks: 24.1 ± 5.2 neuron^{-1} vs. 35.4 ± 6.1 neuron^{-1}, p = 8×10^{-6}). In both cases, *Scn8a* expression decreased by 11 transcripts per neuron.

We monitored $\dot{V}_E$, V_T, and f_R every 3–4 days for 7 weeks in another cohort of VGlut2-ires-cre mice microinjected in the preBötC with AAVs carrying *Scn8a*-targeting (N = 11) and non-targeting control shRNA (N = 7) (Figure S8). Figure 5 and Table 2 present the linear regression analyses for both groups.

$\dot{V}_E$ did not change compared to the baseline values of each group; the slope of both regression lines did not deviate from zero. Additionally, there was no evidence of a treatment effect because the slopes of $\dot{V}_E$ vs. days postinjection did not differ between groups (p = 0.30; Figure 5A). Similarly, V_T remained unaffected following microinjection, and we did not observe a treatment effect between control and *Scn8a*-targeting groups (p = 0.57; Figure 5B).

We observed no changes in f_R for control mice, whereas f_R decreased in the *Scn8a*-targeting group. The change was relatively small (m = −0.30 breaths per min per day, a 5.5% change in f_R overall), and the regression analysis returned a low r^2 (0.035), which means that only 3.5% of the decrease in f_R, the dependent variable, can be attributed to *Scn8a* attenuation, the independent variable. Furthermore, there was no treatment effect when comparing the slopes of f_R vs. days postinjection between groups (p = 0.25; Figure 5C). Given the small r^2, small effect size, and lack of treatment effect, we infer that the decrease in f_R in the *Scn8a*-targeting group is not physiologically meaningful.

We further analyzed T_I, T_E, and V_T/T_I. The itemized linear regression analyses are presented in Figure S9 and Table 2. T_I in the control group decreased following microinjection, but T_I in the *Scn8a*-targeting group did not change. This disparity resulted in a treatment effect between groups (p = 0.02; Figure S9A). Conversely, the control group showed a statistically significant increase in T_E, whereas there was no change in T_E in the *Scn8a*-targeting group. There was no treatment effect regarding T_E (p = 0.4; Figure S9B). The T_I and T_E changes in the control group are small in effect size, and the coefficients of determination are small too. The control group was not subject to gene attenuation, *Scn8a*, or any other known gene because the scrambled nucleotide sequence for the control shRNA does not match any known mouse gene, so we do not consider the changes in T_I and T_E to be physiologically meaningful for evaluating the role of the I_{NaP} or the pacemaker hypothesis. Lastly, we observed no changes in V_T/T_I for either group during the postinjection period, and we did not observe any treatment effect (p = 0.09; Figure S9C).

In addition to $\dot{V}_E$ measurements, we assessed the body and wet lung masses of the *Scn8a*-targeting shRNA-injected and non-targeting shRNA-injected control mice to evaluate whether *Scn8a* manipulation affected general health or pulmonary physiology (Figure S10). The slope of the body mass vs. day postinjection of the *Scn8a*-targeting group deviated from zero (m = 0.062 g d^{-1}, r^2 = 0.077, p = 0.008), but we did not observe a treatment effect compared to its control (p = 0.83) (Figure S10A). Given the lack of treatment effect and the small (7.7%) r^2, it remains unclear how a gain in body mass in these mice could be attributable to *Scn8a* attenuation. Additionally, the wet lung mass did not differ between groups at the end of the study, either unscaled (Figure S10B; p = 0.95) or scaled to body mass (Figure S10C; p = 0.74), suggesting no major differences in pulmonary tissue.

DISCUSSION

The preBötC contains the essential microcircuits for inspiration; *Dbx1*-derived glutamatergic neurons constitute its rhythmogenic core.[2,3,43,44] Knowing the site and cellular point of origin for inspiratory breathing movements is important, but a comprehensive explanation of the behavior must address the cellular- and ion-channel-level mechanisms of rhythmogenesis. Since the discovery of the preBötC, there has been consistent enthusiasm for a rhythmogenic mechanism that depends on the I_{NaP} and bursting-pacemaker neurons, i.e., the pacemaker hypothesis. In its contemporary form, the pacemaker hypothesis acknowledges an integral role for excitatory synaptic interactions to synchronize bursting-pacemaker neurons and to modify their collective dynamics but, nonetheless, is predicated on an essential rhythmogenic role for the I_{NaP}.

Evaluating the pacemaker hypothesis has been fraught with controversy because of experimental caveats and limitations associated with drugs that antagonize the I_{NaP}. Here, rather than fine-tune drug application protocols or relitigate debates about how to interpret drug-based experiments with mixed outcomes, we sought an alternative approach to test the pacemaker hypothesis that avoids the inherent limitations and ambiguities of pharmacology. We employed genetic technologies that reduce or eliminate the Na$^+$ channel isoform giving

rise to the I_{NaP} in core preBötC neurons without off-target effects on other ion channel types or excitatory synaptic transmission.

The widely disseminated report describing the preBötC showed that a subset of its constituent interneurons expresses voltage-dependent bursting properties, which the authors described as "consistent with the hypothesis that conditional bursting-pacemaker neurons are the kernel for rhythmogenesis." Nevertheless, that statement was accompanied by a proviso regarding what evidence would constitute proof that pacemaker neurons are rhythmogenic in neonates and an acknowledgment that developmental changes might modify the rhythmogenic mechanism in adult animals.[4] The present study, besides evaluating the pacemaker hypothesis in its original and contemporary forms, also addresses the developmental criterion.

We measured inspiratory rhythm in slices from *Scn8a* conditional knockout mice to evaluate the first criterion, i.e., whether pacemaker neurons are rhythmogenic neonatally. Two ionic mechanisms underlie bursting-pacemaker activity in preBötC neurons. The first is the I_{NaP}, and the second is the Ca^{2+}-activated non-specific cationic current (I_{CAN}).[4,10,13,14,18,19,45] We now know that the I_{CAN}, mediated by Trpm4 ion channels, is important for motor output pattern rather than for rhythmogenesis.[19,46,47] Therefore, we confined our analysis to the role of the I_{NaP}, targeting $Na_V1.6$ channels encoded by *Scn8a* that constitute the I_{NaP} in many neuron types,[26,28,29] including core preBötC neurons.[15,33,35]

We deleted *Scn8a* from *VGlut2*-expressing neurons, which are synonymous with Dbx1 neurons in the preBötC and form its rhythmogenic core. Voltage-clamp analyses in glutamatergic neurons showed 41% and 66% reductions in the I_{NaP} for single and double *Scn8a* allele deletion, respectively. Our results are commensurate with previous reports showing 67%–76% reduction of the I_{NaP} in *Scn8a* mutant and null mice.[28,31,48] According to the canonical mathematical model, also reproduced here, a preBötC pacemaker neuron does not exhibit bursting following 41% or 66% reduction in the I_{NaP}. However, there is some persistent inward current in glutamatergic preBötC neurons following double *Scn8a* allele deletion, and we propose that the residual current is most likely a "window" current generated by non-$Na_V1.6$ channel isoforms. Indeed, the window current is truly persistent, as it results from the overlap of steady-state activation and inactivation curves. Nonetheless, voltage-dependent bursting requires rapid (on the order of 1–10 ms) subthreshold I_{NaP} activation followed by its slow inactivation (on the order of 300–1,000 ms). Therefore, the window current, without the requisite voltage- and time-dependent properties, cannot contribute to cyclical initiation and termination of cellular bursts. Rather, the Na^+ window current provides a source of tonic excitability akin to Nalcn channels[49,50] that could influence network excitability and thus rhythmic frequency (we return to this point below).

PreBötC neurons express I_{NaP} ubiquitously,[15,21,51] but bursting-pacemaker activity is sparse because it depends on sufficient I_{NaP} expression as well as the ratio of I_{NaP} relative to the K^+-dominated leak current (I_{Leak}).[11–13,52] We assessed the size of the glutamatergic preBötC neuron subpopulation with bursting-pacemaker properties in rhythmic neonatal *VGlut2;Ai148;Scn8a*$^{+/+}$ mouse slices. Rhythmic fluorescent transients in the absence of synaptic transmission and inspiratory rhythm, which define bursting-pacemaker activity,[37]

were present in 11% of glutamatergic preBötC neurons. Previous estimates reported the pacemaker neuron subpopulation to constitute ~5% (P0–P5 and P8–P10 mice)[14] or 16%–29% (P1–P15 mice)[18,53] of the preBötC. Our data fall within that range. In slices from *VGlut2;Ai148;Scn8a*$^{fl/+}$ mice with only one *Scn8a* allele expressed in glutamatergic neurons, we detected no bursting-pacemaker neurons whatsoever. Those imaging data, as well as patch-clamp analysis in combination with computational modeling, provide unambiguous evidence that *VGlut2;Ai148;Scn8a*$^{fl/+}$ mouse slices are devoid of neurons with bursting-pacemaker activity, regardless of I_{K-leak} expression. Nevertheless, inspiratory rhythm persisted in *VGlut2;Ai148;Scn8a*$^{fl/+}$ mouse slices, which demonstrates that rhythmogenesis does not require I_{NaP}-mediated bursting-pacemaker activity. Strictly speaking, the pacemaker hypothesis should be rejected according to the first criterion.

Nevertheless, the I_{NaP} is relevant because it regulates excitability. Indeed, *VGlut2;Ai148;Scn8a*$^{fl/+}$ mouse slices generated slower inspiratory frequency compared with *VGlut2;Ai148;Scn8a*$^{+/+}$ mouse slices. The most parsimonious explanation is that the I_{NaP} contributes an inward current that depolarizes constituent rhythmogenic neurons and that the net effect is to increase the frequency of inspiratory rhythm.

We also evaluated the pacemaker hypothesis from the perspective of the second criterion described above, which addresses the potential for developmental changes in rhythmogenic mechanisms.

The conditional knockout approach deleted *Scn8a* (Na$_V$1.6) from Dbx1 neurons. The clearest effects were on $\dot{V}_E$ and the $\dot{V}_E/\dot{V}_{O_2}$, which increased during postnatal development in all the groups. However, the increase was incommensurate such that *Dbx1;Scn8a*$^{fl/fl}$ mice lacking *Scn8a* in Dbx1 neurons increased $\dot{V}_E$ and $\dot{V}_E/\dot{V}_{O_2}$ at a lower rate compared with *Dbx1;Scn8a*$^{fl/+}$ and *Dbx1;Scn8a*$^{+/+}$ mice with one or both copies of *Scn8a* in Dbx1 neurons. We conclude that the I_{NaP} plays the same role that we identified in slices, depolarizing rhythmogenic preBötC neurons, but *in vivo*, the net effect is to enhance $\dot{V}_E$ and air convection rather than frequency per se. These key respiratory variables still develop but not as robustly as when one or both *Scn8a* alleles are expressed.

F_R did not change for any group during development. T_I did not change either. $\dot{V}_{O_2}$ decreased in wild-type mice but did not change in mice with single or double *Scn8a* deletions in Dbx1 neurons. We can offer no coherent interpretation for these latter data since the change in $\dot{V}_{O_2}$ occurred in the control group only. T_E did not change in control mice; it decreased in single *Scn8a* knockout mice, yet it increased in double *Scn8a* knockout mice. Again, it is challenging to find a coherent interpretation for these data since the effects of removing one vs. two alleles are in opposition. Unaccompanied by changes in f_R and T_I, it is impossible to attribute changes in T_E to modification of *Scn8a* and attendant cellular properties of preBötC neurons. There was no effect of genotype with respect to V_T/T_I, so the increase in V_T/T_I during development for *Dbx1;Scn8a*$^{fl/+}$ and *Dbx1;Scn8a*$^{fl/fl}$ mice cannot be attributed to manipulation of *Scn8a* expression in Dbx1 neurons.

During juvenile to adult stages of development, *Dbx1;Scn8a$^{fl/fl}$* mice developed a severe locomotor phenotype partially reminiscent of allelic *Scn8a* mutations[54,55] that nullify Na$_V$1.6 expression and cause hindlimb ataxia and discoordination with a failure to thrive. In contrast, *Dbx1;Scn8a$^{fl/+}$* mice showed no abnormal locomotor phenotype and grew at a rate commensurate with *Dbx1;Scn8a$^{+/+}$* mice and the background C57BL/6 strain from the Jackson Laboratory (JAX). Germline *Scn8a* mutations affect motoneurons and muscles, whereas our conditional knockout model only affects Dbx1 interneurons. The locomotor phenotype in *Dbx1;Scn8a$^{fl/fl}$* mice probably results from deficits in excitability and repetitive spiking capabilities in Dbx1-derived canonical V0 neurons of the lumbar spinal cord that govern left-right stepping movements, although our mice exhibited hyperextension of the hindlimbs rather than a hopping gait.[56,57] A thorough analysis of the locomotor phenotype is beyond the scope of this report focused on breathing-related consequences of conditional *Scn8a* deletion. Because the surviving pups were able to breathe throughout development, the failure to thrive and the elevated risk of premature death are likely attributable to deficits of locomotion and sensorimotor integration rather than to respiratory insufficiency, although the diminished developmental increase in $\dot{V}_E$ and air convection could only exacerbate morbidity and mortality in *Dbx1;Scn8a$^{fl/fl}$* mice.

The conditional knockdown approach attenuates *Scn8a* (Na$_V$1.6) in glutamatergic neurons limited to the area of virus injection, which avoids the caveat of affecting Dbx1 neurons in the spinal cord and higher brain. Conditional knockdown is also advantageous because the perturbation occurs at the adult stage, when the preBötC is already fully developed. The downside is that knockdown is incomplete; *Scn8a* expression is diminished but not eliminated. RNAscope quantification indicated that shRNA-mediated *Scn8a* knockdown exceeds 40%, which is sufficient I_{NaP} reduction to preclude bursting-pacemaker activity in preBötC neurons, as mathematical modeling and imaging in *VGlut2;Ai148;Scn8a$^{fl/+}$* slices demonstrated.

Adult mice injected with *Scn8a*-targeting shRNA showed no perturbations of any breathing variables. The injected AAV volumes infected glutamatergic neurons throughout the entire preBötC, even spilling out beyond its borders, so we are confident that negative behavioral results cannot be attributed to insufficient infection of glutamatergic preBötC neurons. In fact, a potential caveat is infection of neurons within the intermediate reticulation dorsal to preBötC including inspiratory-related hypoglossal premotor neurons[42,58] and whisking oscillator neurons intimately linked with breathing.[59,60] Any form of ataxic breathing in this context could stem from shRNA effects that diminish excitability of hypoglossal premotor neurons and thus impede airway patency. This was not the case, however; we did not observe any breathing-related ataxia.

Neither conditional knockout nor knockdown affected breathing frequency, in contrast to the slice experiments where single-copy *Scn8a* elimination in Dbx1 neurons slowed down inspiratory rhythm. Why the disparity *in vivo*? Excitatory inputs to the preBötC coming from numerous regions of the intact brain[61] can elevate baseline excitability and are active in unanesthetized mice but absent in slices. Further, the preBötC receives feedback from central and peripheral chemoreceptors *in vivo* that also elevate excitability.[2,62] In awake mice, the removal of *Scn8a* and thus the I_{NaP} is probably too small a perturbation to affect

breathing frequency in comparison to other active inputs and sensory feedback that regulate preBötC excitability and thus maintain breathing frequency. In slices, the contributions of the *Scn8a*-mediated I_{NaP} to baseline excitability, and thus frequency, are more apparent.

What crucial function(s) might the I_{NaP} and bursting-pacemaker activity provide to the preBötC and brainstem breathing-related microcircuits? First, the I_{NaP} in core preBötC neurons is required for normal augmentation of $\dot{V}_E$ and air convection during postnatal development. Second, the present study does not exclude the possibility that the I_{NaP} may be essential in a context where either cellular pacemaker properties or an additional enhancement in excitability is necessary to keep breathing viable, like in gasping.[63] In this interpretive framework, the I_{NaP} and cellular pacemaker properties could be considered redundant rhythmogenic support mechanisms available to be recruited outside of normal physiological circumstances. Third, a rhythmogenic network dubbed the intermediate reticular oscillator (iRO) exists at the margin of, and partially overlaps, the preBötC. The iRO generates rhythmic cries in neonatal mice, which are well coordinated with breathing and appear to depend on I_{NaP}-dependent bursting-pacemaker activity.[64] Whereas I_{NaP}-mediated bursting-pacemaker neurons were first identified and associated with the inspiratory preBötC, these properties are ubiquitous in the ventral medulla[51] and may in fact be obligatory for rhythmogenesis of neonatal crying rather than breathing per se.

Regarding inspiratory rhythm, we favor an essential emergent-network mechanism of rhythmogenesis in which bursting-pacemaker neurons can be embedded but are not obligatory. The core mechanism probably involves a subset of glutamatergic Dbx1 neurons with common intrinsic membrane properties,[9,65,66] which synchronize during the inter-inspiratory interval, that activate output-pattern-related neurons to form inspiratory bursts[66–68] that ultimately drive inspiratory breathing movements. Even if preBötC bursting-pacemaker neurons are not breathing rhythmogenic, the I_{NaP} may be important to regulate breathing development, produce coordinated cries in neonates, or support or generate rhythmogenesis in different physiological contexts, as well as influence baseline excitability —in conjunction with other sources of drive—in the preBötC under normal physiological conditions.

Limitations of the study

Cre-Lox recombination in Dbx1;Scn8a conditional knockout mice affects *Dbx1*-derived cells throughout the CNS, leading to locomotor deficits that ultimately impaired normal growth. Consequently, it was impossible to record $\dot{V}_E$ in ages older than P21 because homozygous *Dbx1;Scn8a^{fl/fl}* mice died. That limitation can be offset using a complementary strategy like shRNA-mediated conditional knockdown, targeting the same gene but only in the intended preBötC core neuron population. This approach also has two limitations. First, virus spread to glutamatergic neurons outside the preBötC, some of which have respiratory pattern-related functionality. Second, shRNA knock-down diminished but did not preclude gene expression, yet the effect was enough to significantly reduce *Scn8a* expression. Nevertheless, in tandem, our two complementary experimental approaches refute the long-standing hybrid pacemaker hypothesis of inspiratory rhythmogenesis.

STAR★METHODS

RESOURCE AVAILABILITY

Lead contact—Further information and requests for resources and reagents should be directed to and will be fulfilled by the lead contact, Christopher A. Del Negro (cadeln@wm.edu).

Materials availability—This study did not generate new unique reagents.

Data and code availability

- Patch-clamp, ventilatory and microscopy data reported in this paper will be shared by the lead contact upon request.

- This paper does not report original code.

- Any additional information required to reanalyze the data reported in this work paper is available from the lead contact upon request.

EXPERIMENTAL MODEL AND STUDY PARTICIPANT DETAILS

Mice—Animals were housed in colony cages maintained on a 12 h:12 h light/dark cycle with controlled humidity and temperature at 24°C. They were fed *ad libitum* on a standard commercial mouse diet (Teklad Global Diets, Envigo, Indianapolis, IN, USA) with free access to water. Cages were furnished with several forms of enrichment.

The Institutional Animal Care and Use Committee at William & Mary (IACUC-2021–04-20–14958-cadeln) and the Institutional Biosafety Committee (IBC-2019–09-02–13765-mrdegu) approved these protocols, which conform to policies of the Office of Laboratory Animal Welfare (National Institutes of Health), the National Research Council,[71] as well as the ARRIVE guidelines 2.0.[72]

In vivo behavioral experiments—For our conditional knockout model, we crossed *Dbx1*[Cre] mice[38] with mice featuring a floxed allele of *Scn8a*, *Scn8a*^{fl/+}, and *Scn8a*^{fl/fl}, in which *loxP* sites flank the first coding exon of *Scn8a*. The floxed allele generates normal $Na_v1.6$ but following Cre-Lox recombination $Na_v1.6$ is deleted completely.[36] The offspring (Dbx1;Scn8a mice) were housed with their dams up to postnatal (P) day 21 (P21). We measured ventilation in Dbx1;Scn8a male and female mice from the neonatal stage (P0) to early adulthood (P21) in 1-h bouts during which the animals were transiently removed from their home cages.

We also measured ventilation in VGlut2-ires-cre mice of both sexes, all within the age range of 10–14 weeks, after conditional knockdown of the *Scn8a* with a Cre-dependent shRNA virus surgically delivered into the preBötC. These mice express Cre recombinase in glutamatergic neurons. *VGlut2* and *Dbx1* are markers for the same preBötC population.[7,8] Thus, one can use either *Dbx1*[Cre] or VGlut2-ires-cre mice to manipulate inspiratory rhythmogenic neurons of the preBötC.

In vitro *electrophysiology and imaging experiments*—Using intersectional mouse genetics (a Cre-driver crossed with one or more Cre-responder strains), we knocked-out *Scn8a* and expressed a florescent marker in *VGlut2*-expressing neurons. We always employed *Scn8a$^{fl/fl}$* or *Scn8a$^{fl/+}$* mice to delete *Scn8a*. For patch-clamp experiments we additionally used a Cre-responder strain dubbed Ai9 that expresses the fluorescent marker tdTomato. For multi-photon imaging experiments, we additionally used a Cre-responder strain dubbed Ai148 that expresses the genetically encoded Ca^{2+} indicator GCaMP6f.

Therefore, we maintained four distinct lines of double Cre-responders: *Ai9;Scn8a$^{fl/fl}$* and *Ai9;Scn8a$^{fl/+}$* as well as *Ai148;Scn8a$^{fl/fl}$* and *Ai148;Scn8a$^{fl/+}$*. We also maintained a line of *Cre*-driver-and-responder mice: VGlut2-ires-cre;*Scn8a$^{fl/+}$*. The offspring of double Cre-responder mice and Cre-driver-and-responder mice inherited either single- or double-floxed copies of *Scn8a* alleles from each parent. For simplicity, we use the nomenclature VGlut2;Ai9;Scn8a to refer to mice used in patch-clamp experiments and VGlut2;Ai148;Scn8a for mice used in multi-photon imaging experiments. The investigators conducted the experiments blind to mouse genotype.

METHOD DETAILS

Electrophysiology—Mouse pups at P0–2 were anesthetized by hypothermia, consistent with the American Veterinary Medical Association guidelines for euthanasia.[73] We removed the neuraxis from the pons to lower cervical spinal cord within 2 min and submerged it in ice-cold artificial cerebrospinal fluid (aCSF) containing (in mM): 124 NaCl, 3 KCl, 1.5 $CaCl_2$, 1 $MgSO_4$, 25 $NaHCO_3$, 0.5 NaH_2PO_4, and 30 dextrose. The aCSF was aerated continuously with 95% O_2 and 5% CO_2. We trimmed the neuraxis and glued the dorsal surface of the brainstem onto an agar block (exposing the ventral side). The block and brainstem were affixed rostral side up within a vibratome (Campden Instruments 7000 smz-2, Leicester, UK) while perfusing with aerated ice-cold aCSF. We cut a single transverse slice 450–500 μm thick with preBötC on its rostral surface.[41]

Slices from VGlut2;Ai9;Scn8a mice were held in place and perfused with aCSF (28°C) at 2–4 mL min^{-1} in a recording chamber on a fixed-stage upright microscope equipped with a water-immersion objective (63X, 1.0 numerical aperture). The external K^+ concentration ($[K^+]_{ext}$) in the aCSF was raised from 3 to 9 mM, which facilitates robust inspiratory rhythm and XII motor output. We recorded XII motor output using suction electrodes fabricated from borosilicate glass pipettes (OD: 1.2 mm, ID: 0.68 mm) fire-polished to a diameter of ~100 μm. XII motor output was amplified by 2,000 and band-pass filtered (300–1000 Hz).

We identified tdTomato-expressing neurons using epifluorescence microscopy. Then, whole-cell patch-clamp recordings were performed on those neurons while under visual control using infrared-enhanced differential interference contrast microscopy. Patch pipettes with tip resistance of 4–6 MΩ were fabricated from capillary glass (OD: 1.50 mm, ID: 0.86 mm) and filled with solution containing (in mM): 110 CsCl, 5 NaCl, 20 tetraethylammonium-chloride (TEA-Cl), 10 EGTA, 10 HEPES, 1.2 $CaCl_2$. We employed a patch-clamp amplifier (EPC10, HEKA Electronic, Holliston, MA, USA) to record membrane current at a gain of 5x or 10x in voltage clamp. All signals were low pass filtered (1 kHz) and digitally acquired at 4 kHz in PatchMaster software.

Membrane capacitance (C_M) was determined from the integral of the leak-subtracted transient capacity current ($\int I_C$) evoked by a series of 15-ms hyperpolarizing voltage-step commands (V_{com}) applied within 10 mV of holding potential (V_{hold}), using the formula $Q_M = \int I_C$ for each V_{com}. C_M is determined from the slope of the plot of Q_M versus ΔV_M (where ΔV_M is $V_{com} - V_{hold}$) for the series of step commands according to the capacitor law $C_M = V_M \div Q$.

We measured the quasi-steady-state current-voltage (IV) relationship generated by a slow voltage ramp (50 mV/s) between −70 and +10 mV.

Multi-photon imaging—We imaged cytosolic Ca^{2+} concentration in neurons contained in slices from VGlut2;Ai148;Scn8a mice. Similarly, $[K^+]_{ext}$ was raised from 3 to 9 mM and slices were held in place and perfused with aCSF (28°C) at 2–4 mL min^{-1} in a recording chamber on a fixed-stage multi-photon laser-scanning confocal microscope (Thorlabs, Newton, NJ, USA) equipped with a water-immersion objective (20x, 1.0 numerical aperture). Illumination was provided by an ultrafast tunable laser with a power output of 1050 mW at an emission wave-length of 970 nm, where pulse frequency was 80 MHz and pulse duration was 100 fs (Coherent Chameleon Discovery, Santa Clara, CA, USA). We scanned the preBötC in a raster pattern and used a non-descanned photomultiplier tube to detect reflected light, which was digitally reassembled into images via software. Each frame consisted of a two-way raster scan with a resolution of 256×256 pixels (116×116 μm). We collected fluorescence time series data at 15 Hz using ThorImage LS 4.1 software and then analyzed the data using MATLAB 2021a.

To analyze a time series, we first calculated the average fluorescence intensity for all pixels in each frame. Mean fluorescence intensity as a function of time showed periodic network activity. We used the 95% confidence interval (CI) of cycle periods to define the high frequency (short cycle period) and low frequency (long cycle period) limits of a window in frequency space. Next, we performed fast Fourier transforms of the time series for each pixel. The maximum power from the previously defined window in frequency space was mapped to the corresponding pixel in a new, processed two-dimensional image.

We calculated the mean and standard deviation of the power from each pixel in the new processed image. Rhythmically active pixels exhibited power far greater than the average. Therefore, all pixels with intensity less than mean +2 standard devations(SDs) were set to zero. The remaining contiguous pixel sets, whose area exceeds 8 μm^2, were retained as regions of interest (ROIs). The Ca^{2+} fluoresce changes within those ROIs, obtained from the original time series, were calculated using the equation $\frac{(F_i - F_o)}{F_o}$, i.e., $\frac{\Delta F}{F_o}$ where F_i is the instantaneous average fluorescence intensity for all pixels within a given ROI and F_o is the average fluorescence intensity of all pixels within that same ROI averaged over the entire time series.

Simulations—We simulated the preBötC neuron model by Butera and colleagues,[11] specifically model 1 that features a slowly inactivating I_{NaP}. The equations are fully listed in

the original publication. Numerical integration was performed by MATLAB (ode45) running a Runge-Kutta 4 method with a variable time step.

Ventilation measurements

Neonatal to juvenile mice: We measured ventilation $\left(\dot{V}_E\right)$ in neonatal (P0–9) and juvenile (P12–18) Dbx1;Scn8a mice using a dual-chamber barometric method, which is advantageous for newborn animals with limited thermogenesis.[74] Two chambers made of graduated syringes were inter-connected via a polyethylene tube. The first chamber housed the mouse and was kept in a water bath to maintain an internal temperature of ~37°C, measured by a temperature sensing transponder (BioTherm13, Biomark, Idaho, USA). The second reference chamber was kept outside of the water bath at room temperature (~25°C), having its temperature measured by a digital thermometer, and was connected to a differential pressure transducer (Spirometer, ADInstruments, Colorado Springs, CO, USA) to measure breathing-related pressure oscillations. We adjusted chamber size by moving the syringe plunger to fit closely to the body: 9 mL for mice at age P0, 10 mL at P3–5, 12 mL at P7–9, 25 mL at P12, and 30 mL at P15–18. Air flow through the chambers was maintained at 80 mL min^{-1} for mice at ages P0–9, 100 mL min^{-1} for mice at age P12, and 120 mL min^{-1} for mice at age P15–18, controlled via the suction pump of a gas analyzer (ADInstruments) and measured using a flowmeter (PFMV530–1, SMCpneumatics, Noblesville, IN, USA) in series with the gas analyzer. Pressure changes due to breathing were sampled at 1 kHz by a PowerLab (ADInstruments) analog-to-digital converter for digital storage and analysis. Mice were placed in the first chamber for a minimum acclimation period of 30 min $\dot{V}_E$ was measured at 30, 40, and 50 min of elapsed time, where the airflow was interrupted for 2 min and the chamber open only to the pressure transducer. The average of the 3 bouts was reported. Calibration of the tidal volume was done by injecting a known volume of air in the first chamber after the third recording bout.

Early adulthood and adult mice: We measured $\dot{V}_E$ in P21 and adult mice (10–14 weeks old) using flow-through whole-body plethysmography.[75] A 300 mL experimental chamber (SCIREQ, Emka Technologies, Qué bec, Canada) was ventilated with an air mixture (21% O_2 and N_2 balance). Inlet flow was maintained at 250 mL min^{-1}, controlled by a flowmeter, and outlet flow was maintained at 250 mL min^{-1} by a suction pump coupled to the chamber. A fractional leak was introduced into this system to provide better control of the pressure inside the chamber. Thus, this system behaved as if it were sealed for time varying signals with frequency exceeding 0.5 Hz.[74–76] Body temperature was measured by an indwelling sensor (BioTherm13), ambient temperature was measured by a general-purpose liquid-in-glass thermometer, and chamber temperature was monitored using a digital thermometer. The chamber was connected to a differential pressure transducer to measure pressure oscillations due to breathing, which were sampled at 1 kHz by a PowerLab for storage and analysis. Mice were placed in the chamber for a minimum acclimation period of 30 min. $\dot{V}_E$ was recorded continuously for additional 30 min. We analyzed 3 bouts of 2 min each and averaged them.

For neonatal (P0–9), juvenile (P12–18), early adulthood (P21) and adult (10–14 weeks old) experiments, we measured two respiratory variables: respiratory frequency (f_R, in

breaths per minute, i.e., bpm) and tidal volume (V_T, in mL), the latter calculated using the Drorbaugh-Fenn[77] formula:

$$V_T = \frac{V_K\left(\frac{P_T}{P_K}\right) \times T_B(P_B - P_C)}{T_B(P_B - P_C) - T_A(P_B - P_R)}$$

where V_T is the tidal volume; V_K is the volume of air injected into the animal chamber for calibration; P_T is the pressure deflection associated with the volume of breathed air; P_K is the pressure deflection associated V_K; T_B is body temperature (in Kelvin, K); P_B is barometric pressure (in mm Hg); P_C is the vapor pressure of water in the animal chamber (in mm Hg); T_A is the air temperature inside the chamber; and P_R is the water vapor pressure at T_B. We present V_T with respect to body mass as a fraction of 100 g. We obtained P_C and P_R from an appropriate lookup table.

$\dot{V}_E$ was calculated as the product of f_R and $V_T \cdot \dot{V}_E$ and V_T were reported at T_B and ambient barometric pressure, presuming that the air was fully saturated with water vapor (BTPS, stands for Body Temperature, Pressure, water Saturated). For neonatal mice, the V_K was typically a step volume change of 0.15 mL. For juvenile and adult mice, V_K was typically 0.3 mL delivered in 5 sets of 20 oscillatory injections at a rate matching the breathing frequency.

Metabolic measurements—Metabolic rate was inferred by indirect calorimetry, which consisted of measuring oxygen consumption $(\dot{V}_{O_2})$ in an open respirometry system using a flow-through (pull mode), configuration where air is drawn into a gas analyzer (ADInstruments).[78,79] For the dual-chamber system used for neonatal (P0–9) and juvenile mice (P12–18), flow to the gas analyzer was 80, 100, or 120 mL.min^{-1-} depending on age. For the flow-through whole-body plethysmography used for P21 and adult mice, flow to the gas analyzer was 120 mL min^{-1}. In both configurations, the air was dried through a 10-cm Drierite column (W.A. Hammond Drierit Co. Ltd, Xenia, OH, USA) before passing through the analyzer. We calibrated the gas analyzer using standard room air (20.95% O_2 and 0.03% CO_2) and carbogen mixture (95% O_2 and 5% CO_2). Air was continuously sampled by the gas analyzer and digitally acquired at 1 kHz by PowerLab and LabChart software.

Oxygen consumption was calculated using the following formula[80]:

$$\dot{V}_{O_2} = \frac{Fl \times (F_{iO_2} - F_{eO_2})}{(1 - F_{iO_2}) \times (1 - RQ)}$$

where Fl is the input flow rate, F_{iO_2} is fraction of inspired O_2; F_{eO_2} is the fraction of expired O_2. The respiratory quotient (RQ) is the ratio of carbon dioxide released to oxygen consumed $\frac{V_{CO_2}}{\dot{V}_{O_2}}$, which is generally 0.85 for standard mouse diet. The $\dot{V}_{O_2}$ is expressed as a fraction of 100 g under Standard conditions of Temperature, Pressure, and Dry air (STPD).

Surgical procedures

shRNA injections in the preBötC: We administered a Cre-dependent Adeno-associated virus of serotype 9 (AAV9) carrying an FLEX (flip-excision) construct with a synapsin promoter, and mCherry fluorescent protein for glutamatergic neuron identification, on a miR30 backbone.[81,82] The virus also carried a short hairpin RNA (shRNA) targeting 3 sequences of *Scn8a* mouse gene (NCBI Gene ID: 20273): TTGTCCTGAACACACTATTTA; CTTCGACTGGGAGGAGTATAT; TGCCTTGAGACACTACTATTT. Recombination occurred in the presence of Cre, which reversed the sequences and led to mCherry and shRNA expression.

Mice were anesthetized via isoflurane (5% v/v for induction, and 2% v/v for maintenance), and positioned in a stereotaxic frame. The skull was exposed, aseptically cleaned, and then two holes were drilled at the coordinates: −6.9–6.8 mm caudal to bregma, ±1.2 mm lateral to midline, at a depth of −5.2 mm from the brain surface.[47] We injected 50 nL of the virus into the preBötC using a 30-gauge 0.5 μL Hamilton Neurosyringe (Hamilton Company, Reno, NV, USA).

Implantation of temperature sensors: We monitored body temperature of P21 mice and adult (10–14 weeks old) mice using a temperature sensing transponder (BioTherm 13) with dimensions 2.12 mm × 13 mm. We inserted the probe in the abdominal cavity via laparotomy after isoflurane anesthesia (5% v/v for induction, and 2% v/v for maintenance), and shaving and cleaning the skin with chlorhexidine (2%) and alcohol (70%). The procedure was completed in 10 min.

Molecular assays

RNAscope: We used RNAscope Multiplex Fluorescent V2 Assay (Advanced Cell Diagnostics, i.e., ACDBio, Newark, CA, USA) to assess the expression of *Scn8a* transcripts in juvenile Dbx1;Scn8a and adult VGlut2-ires-cre injected mice. Mice were deeply anesthetized with isoflurane, then perfused through the right atrium with a phosphate-buffered saline solution (PBS) 0.1x, followed by 4% paraformaldehyde (PFA). Their brains were removed and kept in 4% PFA at 4°C overnight (~18 h). For Dbx1;Scn8a mice, fixed brains where sectioned at 30 μm using a vibratome and only 3 sections/animal at bregma levels −7.04 mm, −6.92 mm and −6.8 mm were used for RNAscope. Sections were then saved in a well plate with Tris-buffered saline solution with Tween 20 (TBST) 0.5x, for maximum of 48 h at 4°C and then used for multiplex *in situ* hybridization. For VGlut2-ires-cre mice, we also used fixed brains sectioned at 30 μm in duplicate through the preBötC. The first duplicate section was used to assess virus expression (mCherry) under the fluorescent microscope (Axioscope 5 Upright Microscope, Zeiss). The second duplicate section was saved in a well plate with TBST 0.5x, for maximum of 48 h at 4°C and then used for multiplex *in situ* hybridization. Assays for Dbx1;Scn8a and VGlut2-ires-cre were not run concurrently.

Slices from Dbx1;Scn8a and VGlut2-ires-cre mice were pre-treated equally and followed the same RNAscope protocol. On the first day, sections were washed in TBST 0.5x, mounted onto superfrost slides, and then subjected to a pre-treatment protocol for fixation,

dehydration, and target recovery. On the second day, slices were incubated with protease plus for 30 min at 40°C and then incubated in RNAscope oligonucleotide probes for their respective genes of interest, for 2 h at 40°C. For Dbx1;Scn8a samples, we used probes for *Scn8a* and *Even-skipped homeobox 1* (*Evx1*), the latter being a post-mitotic cell marker for Dbx1 neurons. For VGlut2-ires-cre injected mice, we used probes for *Scn8a* and mCherry, the latter being used to identify transduced glutamatergic neurons. Tissues were then processed using the Multiplex Fluorescent Reagent Kit V2 Assay (ACDBio). Fluorescent probes Opal 520 (1:1500), *for Scn8a*, and Opal 690 (1:1500), for *Evx1* and mCherry, were also used. Finally, slides were incubated for 30 s with DAPI, covered with ProLong Gold Antifade Mountant (Invitrogen, Waltham, MA), and coverslipped.

Sections were visualized under the four channel, upright laser-scanning confocal microscope (Cerna, ThorLabs) using a 40× objective (numerical aperture 0.25 μm), and images were acquired using the ThorImage LS 4.1 software.

***Genotyping mice (*Scn8a^fl/+^, Scn8a^fl/fl^, Dbx1^Cre^, *and Vglut2-ires-cre)*:** Genomic DNA from ear or tail was collected and PCR was used to assess genotype. For *Scn8a^fl/+^* and *Scn8a^fl/fl^* mice, two primers were used: forward: GTG TGT GAT TCT CAA CAG TGG GTT, and reverse: GTC TGT AAG AAG GCC TGA AAG TGA. For *Dbx1^Cre^* mice, we used one primer for the wild-type allele: forward: GAG GAT GAG GAA ATC ACG GTG, and reverse: GCA AGG AAA TGT CTC TGG GAC; For the mutant Cre allele, the following primers were used: forward: GTC CAA TTT ACT GAC CGT ACA CC, and reverse: GTT ATT CGG ATC ATC AGC TAC ACC. For VGlut2-ires-cre mice, we used the primers forward: CGG TAC CAC CAA ATC TTA CGG, CAT GGT CTG TTT TGA ATT CAG and reverse: ATC GAC CGG TAA TGC AGG CAA.

QUANTIFICATION AND STATISTICAL ANALYSIS

Ventilation of Dbx1;Scn8a and Vglut2-ires-cre mice—We plotted respiratory measurements as a function of post-natal age or days post-shRNA injection. We performed linear-regression analyses to obtain the best-fit slope (m) and coefficient of determination (r^2) along with the 95% CIs for each relationship (Graphpad Prism, La Jolla, CA). We used an F-test to evaluate the slope of the respiratory measures versus age or day post-shRNA. If there is no relationship, i.e., slope is zero, then the F statistic returns a *p* value quantifying the likelihood of obtaining a slope deviating from zero.

Body and lung mass—We recorded the body mass of the mice every day before recording ventilation. We plotted their body mass as a function of post-natal age or days post-shRNA injection, performing linear regression analyses as described above. We removed and weighed the lungs of VGlut2-ires-cre mice on the last day of experiments. Differences between lung masses of experimental groups were evaluated using an unpaired Student's t-test.

mRNA quantification for Vglut2-ires-cre mice and site of injection—The amount of mRNA per glutamatergic preBötC neuron in VGlut2-ires-cre mice was assessed using the open-source software Quantitative Pathology (QuPath).[69] mCherry expression was used

to delineate the borders of glutamatergic neurons for subsequent transcript quantification. Each dot inside of a mCherry-positive neuron represents a single transcript. The threshold for detection of cells and transcripts remained fixed throughout the analyzes. We quantified the transcripts on ~6 non-overlapping images per section. Approximately 17 neurons were captured in each picture. Those images were analyzed separately and then averaged, forming one data point per section. We analyzed ~9 sections per mouse and the transcript count for each section was plotted in a univariate scatterplot with the effect size (difference between means) and its 95% confidence interval, i.e., estimation statistics,[83] which includes an unpaired t test.

The extent of virus expression was evaluated in VGlut2-ires-cre mice. Transverse sections of the brainstem were imaged in a 6×4 array at 10× magnification. Tiles were then reassembled using open-source software ImageJ.[70] The virus expression area on sections from individual mice were superimposed onto a section redrawn from the adult mouse brain atlas.[40]

For all statistical tests we applied a significance threshold of $a = 0.05$. Means are reported ± SD.

Supplementary Material

Refer to Web version on PubMed Central for supplementary material.

ACKNOWLEDGMENTS

INCLUSION AND DIVERSITY

We worked to ensure sex balance in the selection of non-human subjects. One or more of the authors of this paper self-identifies as an underrepresented ethnic minority in their field of research or within their geographical location. One or more of the authors of this paper self-identifies as a gender minority in their field of research. One or more of the authors of this paper self-identifies as a member of the LGBTQIA+ community. While citing references scientifically relevant for this work, we also actively worked to promote gender balance in our reference list. We avoided "helicopter science" practices by including the participating local contributors from the region where we conducted the research as authors on the paper.

REFERENCES

1. Feldman JL, and Kam K (2015). Facing the challenge of mammalian neural microcircuits: taking a few breaths may help. J. Physiol. 593, 3–23. 10.1113/jphysiol.2014.277632. [PubMed: 25556783]

2. Del Negro CA, Funk GD, and Feldman JL (2018). Breathing matters. Neuroscience 19, 351–367. 10.1038/s41583-018-0003-6. [PubMed: 29740175]

3. Ashhad S, Kam K, Del Negro CA, and Feldman JL (2022). Breathing rhythm and pattern and their influence on emotion. Annu. Rev. Neurosci. 45, 223–247. 10.1146/ANNUREV-NEURO-090121-014424. [PubMed: 35259917]

4. Smith JC, Ellenberger HH, Ballanyi K, Richter DW, and Feldman JL (1991). Pre-Bötzinger complex: a brainstem region that may generate respiratory rhythm in mammals. Science 254, 726–729. 10.126/science.1683005. [PubMed: 1683005]

5. Funk GD, Smith JC, and Feldman JL (1993). Generation and transmission of respiratory oscillations in medullary slices: role of excitatory amino acids. J. Neurophysiol. 70, 1497–1515. 10.1152/jn.1993.70.4.1497. [PubMed: 8283211]

6. Wallé n-Mackenzie A, Gezelius H, Thoby-Brisson M, Nygård A, Enjin A, Fujiyama F, Fortin G, and Kullander K. (2006). Vesicular glutamate transporter 2 is required for central respiratory rhythm generation but not for locomotor central pattern generation. J. Neurosci. 26, 12294–12307. 10.1523/JNEUROSCI.3855-06.2006. [PubMed: 17122055]

7. Bouvier J, Thoby-Brisson M, Renier N, Dubreuil V, Ericson J, Champagnat J, Pierani A, Chédotal A, and Fortin G (2010). Hindbrain interneurons and axon guidance signaling critical for breathing. Nat. Neurosci. 13, 1066–1074. 10.1038/nn.2622. [PubMed: 20680010]

8. Gray PA, Hayes JA, Ling GY, Llona I, Tupal S, Picardo MCD, Ross SE, Hirata T, Corbin JG, Eugenín J, et al. (2010). Developmental origin of pre-Botzinger Complex respiratory neurons. J. Neurosci. 30, 14883–14895. 10.1523/JNEUROSCI.4031-10.2010. [PubMed: 21048147]

9. Picardo MCD, Weragalaarachchi KTH, Akins VT, and Del Negro CA (2013). Physiological and morphological properties of Dbx1-derived respiratory neurons in the pre-Bötzinger Complex of neonatal mice. J. Physiol. 591, 2687–2703. 10.1113/jphysiol.2012.250118. [PubMed: 23459755]

10. Johnson SM, Smith JC, Funk GD, and Feldman JL (1994). Pacemaker behavior of respiratory neurons in medullary slices from neonatal rat. J. Neurophysiol. 72, 2598–2608. 10.1152/JN.1994.72.6.2598. [PubMed: 7897477]

11. Butera RJ, Rinzel J, and Smith JC (1999). Models of respiratory rhythm generation in the pre-Bötzinger Complex. I. Bursting pacemaker neurons. J. Neurophysiol. 82, 382–397. 10.1152/JN.1999.82.1.382. [PubMed: 10400966]

12. Koizumi H, and Smith JC (2008). Persistent Na+ and K+-dominated leak currents contribute to respiratory rhythm generation in the pre-Bötzinger Complex in vitro. J. Neurosci. 28, 1773–1785. 10.1523/JNEUROSCI.3916-07.2008. [PubMed: 18272697]

13. Del Negro CA, Koshiya N, Butera RJ, and Smith JC (2002). Persistent sodium current, membrane properties and bursting behavior of pre-Bötzinger Complex inspiratory neurons in vitro. J. Neurophysiol. 88, 2242–2250. 10.1152/jn.00081.2002. [PubMed: 12424266]

14. Del Negro CA, Morgado-Valle C, Hayes JA, Mackay DD, Pace RW, Crowder EA, and Feldman JL (2005). Sodium and calcium current-mediated pacemaker neurons and respiratory rhythm generation. J. Neurosci. 25, 446–453. 10.1523/JNEUROSCI.2237-04.2005. [PubMed: 15647488]

15. Ptak K, Zummo GG, Alheid GF, Tkatch T, Surmeier DJ, and McCrimmon DR (2005). Sodium currents in medullary neurons isolated from the pre-Bötzinger Complex region. J. Neurosci. 25, 5159–5170. 10.1523/JNEUROSCI.4238-04.2005. [PubMed: 15917456]

16. Yamanishi T, Koizumi H, Navarro MA, Milescu LS, and Smith JC (2018). Kinetic properties of persistent Na+ current orchestrate oscillatory bursting in respiratory neurons. J. Gen. Physiol. 150, 1523–1540. 10.1085/jgp.201812100. [PubMed: 30301870]

17. Del Negro CA, Morgado-Valle C, and Feldman JL (2002). Respiratory rhythm: an emergent network property? Neuron 34, 821–830. 10.1016/s0896-6273(02)00712-2. [PubMed: 12062027]

18. Peña F, Parkis MA, Tryba AK, and Ramirez JM (2004). Differential contribution of pacemaker properties to the generation of respiratory rhythms during normoxia and hypoxia. Neuron 43, 105–117. 10.1016/j.neuron.2004.06.023. [PubMed: 15233921]

19. Phillips RS, Koizumi H, Molkov YI, Rubin JE, and Smith JC (2022). Predictions and experimental tests of a new biophysical model of the mammalian respiratory oscillator. Elife 11, 74762. 10.7554/ELIFE.74762.

20. Chevalier M, Toporikova N, Simmers J, and Thoby-Brisson M (2016). Development of pacemaker properties and rhythmogenic mechanisms in the mouse embryonic respiratory network. Elife 5, e16125. 10.7554/ELIFE.16125. [PubMed: 27434668]

21. Pace RW, Mackay DD, Feldman JL, and Del Negro CA (2007). Role of persistent sodium current in mouse pre-Bötzinger Complex neurons and respiratory rhythm generation. J. Physiol. 580, 485–496. 10.1113/jphysiol.2006.124602. [PubMed: 17272351]

22. MacIver MB, Amagasu SM, Mikulec AA, and Monroe FA (1996). Riluzole anesthesia: use-dependent block of presynaptic glutamate fibers. Anesthesiology 85, 626–634. 10.1097/00000542-199609000-00023. [PubMed: 8853094]

23. Bellingham MC (2011). A review of the neural mechanisms of action and clinical efficiency of riluzole in treating amyotrophic lateral sclerosis: what have we learned in the last decade? CNS. Neurosci. Ther. 17, 4–31. 10.1111/J.1755-5949.2009.00116.X. [PubMed: 20236142]

24. Doble A (1996). The pharmacology and mechanism of action of riluzole. Neurology 47, S233–S241. 10.1212/WNL.47.6_SUPPL_4.233S. [PubMed: 8959995]

25. Phillips RS, and Rubin JE (2019). Effects of persistent sodium current blockade in respiratory circuits depend on the pharmacological mechanism of action and network dynamics. PLoS Comput. Biol. 15, e1006938. 10.1371/JOURNAL.PCBI.1006938. [PubMed: 31469828]

26. Zybura A, Hudmon A, and Cummins TR (2021). Distinctive properties and powerful neuromodulation of Nav 1.6 sodium channels regulates neuronal excitability. Cells 10, 1595. 10.3390/cells10071595. [PubMed: 34202119]

27. Chen Y, Yu FH, Sharp EM, Beacham D, Scheuer T, and Catterall WA (2008). Functional properties and differential neuromodulation of Nav1.6 channels. Mol. Cell. Neurosci. 38, 607–615. 10.1016/j.mcn.2008.05.009. [PubMed: 18599309]

28. Raman IM, Sprunger LK, Meisler MH, and Bean BP (1997). Altered subthreshold sodium currents and disrupted firing patterns in Purkinje neurons of Scn8a mutant mice. Neuron 19, 881–891. 10.1016/s0896-6273(00)80969-1. [PubMed: 9354334]

29. Smith MR, Smith RD, Plummer NW, Meisler MH, and Goldin AL (1998). Functional analysis of the mouse Scn8a sodium channel. J. Neurosci. 18, 6093–6102. 10.1523/JNEUROSCI.18-16-06093.1998. [PubMed: 9698304]

30. Enomoto A, Han JM, Hsiao CF, and Chandler SH (2007). Sodium currents in mesencephalic trigeminal neurons from Nav1.6 null mice. J. Neurophysiol. 98, 710–719. 10.1152/JN.00292.2007. [PubMed: 17522178]

31. Do MTH, and Bean BP (2004). Sodium currents in subthalamic nucleus neurons from Nav1.6-null mice. J. Neurophysiol. 92, 726–733. 10.1152/JN.00186.2004. [PubMed: 15056687]

32. Burbidge SA, Dale TJ, Powell AJ, Whitaker WRJ, Xie XM, Romanos MA, and Clare JJ (2002). Molecular cloning, distribution and functional analysis of the NA(V)1.6. Voltage-gated sodium channel from human brain. Brain Res. Mol. Brain Res. 103, 80–90. 10.1016/S0169-328X(02)00188-2. [PubMed: 12106694]

33. Hayes JA, Kottick A, Picardo MCD, Halleran AD, Smith RD, Smith GD, Saha MS, and Del Negro CA (2017). Transcriptome of neonatal preBötzinger complex neurons in Dbx1 reporter mice. Sci. Rep. 7, 8669. 10.1038/s41598-017-09418-4. [PubMed: 28819234]

34. Kallurkar PS, Picardo MCD, Sugimura YK, Saha MS, Conradi Smith GD, and Del Negro CA (2022). Transcriptomes of electrophysiologically recorded Dbx1-derived respiratory neurons of the preBötzinger Complex in neonatal mice. Sci. Rep. 12, 2923. 10.1038/S41598-022-06834-Z. [PubMed: 35190626]

35. David CK, Sugimura YK, Kallurkar PS, Picardo MCD, Saha MS, Conradi Smith GD, and Del Negro CA (2022). Single cell transcriptome sequencing of inspiratory neurons of the preBötzinger Complex in neonatal mice. Sci. Data 9, 457. 10.1038/S41597-022-01569-Y. [PubMed: 35907922]

36. Levin SI, and Meisler MH (2004). Floxed allele for conditional inactivation of the voltage-gated sodium channel Scn8a (NaV1.6). Genesis 39, 234–239. 10.1002/gene.20050. [PubMed: 15286995]

37. Koshiya N, and Smith JC (1999). Neuronal pacemaker for breathing visualized in vitro. Nature 400, 360–363. 10.1038/22540. [PubMed: 10432113]

38. Bielle F, Griveau A, Narboux-Nême N, Vigneau S, Sigrist M, Arber S, Wassef M, and Pierani A. (2005). Multiple origins of Cajal-Retzius cells at the borders of the developing pallium. Nat. Neurosci. 8, 1002–1012. 10.1038/NN1511. [PubMed: 16041369]

39. Moran-Rivard L, Kagawa T, Saueressig H, Gross MK, Burrill J, and Goulding M (2001). Evx1 is a postmitotic determinant of V0 interneuron identity in the spinal cord. Neuron 29, 385–399. 10.1016/S0896-6273(01)00213-6. [PubMed: 11239430]

40. Paxinos G, and Franklin KBJ (2019). Paxinos and Franklin's the Mouse Brain in Stereotaxic Coordinates, 5th ed. (Academic Press).

41. Ruangkittisakul A, Kottick A, Picardo MCD, Ballanyi K, and Del Negro CA (2014). Identification of the pre-Bötzinger Complex inspiratory center in calibrated "sandwich" slices from newborn mice with fluorescent Dbx1 interneurons. Physiol. Rep. 2, e12111. 10.14814/PHY2.12111. [PubMed: 25138790]

42. Revill AL, Vann NC, Akins VT, Kottick A, Gray PA, Del Negro CA, and Funk GD (2015). Dbx1 precursor cells are a source of inspiratory XII premotoneurons. Elife 4, e12301. 10.7554/eLife.12301. [PubMed: 26687006]

43. Ramirez JM, and Baertsch N (2018). Defining the rhythmogenic elements of mammalian breathing. Physiology 33, 302–316. 10.1152/physiol.00025.2018. [PubMed: 30109823]

44. Ramirez JM, and Baertsch NA (2018). The dynamic basis of respiratory rhythm generation: one breath at a time. Annu. Rev. Neurosci. 41, 475–499. 10.1146/ANNUREV-NEURO-080317-061756. [PubMed: 29709210]

45. Thoby-Brisson M, and Ramirez JM (2001). Identification of two types of inspiratory pacemaker neurons in the isolated respiratory neural network of mice. J. Neurophysiol. 86, 104–112. 10.1152/JN.2001.86.1.104. [PubMed: 11431492]

46. Koizumi H, John TT, Chia JX, Tariq MF, Phillips RS, Mosher B, Chen Y, Thompson R, Zhang R, Koshiya N, et al. (2018). Transient receptor potential channels TRPM4 and TRPC3 critically contribute to respiratory motor pattern formation but not rhythmogenesis in rodent brainstem circuits. eNeuro 5, ENEURO.0332–17.2018. 10.1523/ENEURO.0332-17.2018.

47. Picardo MCD, Sugimura YK, Dorst KE, Kallurkar PS, Akins VT, Ma X, Teruyama R, Guinamard R, Kam K, Saha MS, et al. (2019). Trpm4 ion channels in pre-Bötzinger Complex interneurons are essential for breathing motor pattern but not rhythm. PLoS Biol. 17, e2006094. 10.1371/JOURNAL.PBIO.2006094. [PubMed: 30789900]

48. Maurice N, Tkatch T, Meisler M, Sprunger LK, and Surmeier DJ (2001). D1/D5 dopamine receptor activation differentially modulates rapidly inactivating and persistent sodium currents in prefrontal cortex pyramidal neurons. J. Neurosci. 21, 2268–2277. 10.1523/JNEUROSCI.21-07-02268.2001. [PubMed: 11264302]

49. Ren D (2011). Sodium leak channels in neuronal excitability and rhythmic behaviors. Neuron 72, 899–911. 10.1016/J.NEURON.2011.12.007. [PubMed: 22196327]

50. Lu B, Su Y, Das S, Liu J, Xia J, and Ren D (2007). The neuronal channel NALCN contributes resting sodium permeability and is required for normal respiratory rhythm. Cell 129, 371–383. 10.1016/J.CELL.2007.02.041. [PubMed: 17448995]

51. Rybak IA, Ptak K, Shevtsova NA, and McCrimmon DR (2003). Sodium currents in neurons from the rostroventrolateral medulla of the rat. J. Neurophysiol. 90, 1635–1642. 10.1152/JN.00150.2003. [PubMed: 12761275]

52. Purvis LK, Smith JC, Koizumi H, and Butera RJ (2007). Intrinsic bursters increase the robustness of rhythm generation in an excitatory network. J. Neurophysiol. 97, 1515–1526. 10.1152/JN.00908.2006. [PubMed: 17167061]

53. Pagliardini S, Adachi T, Ren J, Funk GD, and Greer JJ (2005). Fluorescent tagging of rhythmically active respiratory neurons within the pre-Bötzinger Complex of rat medullary slice preparations. J. Neurosci. 25, 2591–2596. 10.1523/JNEUROSCI.4930-04.2005. [PubMed: 15758169]

54. Meisler MH, Plummer NW, Burgess DL, Buchner DA, and Sprunger LK (2004). Allelic mutations of the sodium channel SCN8A reveal multiple cellular and physiological functions. Genetica 122, 37–45. 10.1007/s10709-004-1441-9. [PubMed: 15619959]

55. Meisler MH, Kearney J, Escayg A, MacDonald BT, and Sprunger LK (2001). Sodium channels and neurological disease: insights from Scn8a mutations in the mouse. Neuroscientist 7, 136–145. 10.1177/107385840100700208. [PubMed: 11496924]

56. Talpalar AE, Bouvier J, Borgius L, Fortin G, Pierani A, and Kiehn O (2013). Dual-mode operation of neuronal networks involved in left–right alternation. Nature 500, 85–88. 10.1038/nature12286. [PubMed: 23812590]

57. Kiehn O (2016). Decoding the organization of spinal circuits that control locomotion. Nat. Rev. Neurosci. 17, 224–238. 10.1038/nrn.2016.9. [PubMed: 26935168]

58. Koizumi H, Wilson CG, Wong S, Yamanishi T, Koshiya N, and Smith JC (2008). Functional imaging, spatial reconstruction, and biophysical analysis of a respiratory motor circuit isolated in vitro. J. Neurosci. 28, 2353–2365. 10.1523/JNEUROSCI.3553-07.2008. [PubMed: 18322082]

59. Takatoh J, Prevosto V, Thompson PM, Lu J, Chung L, Harrahill A, Li S, Zhao S, He Z, Golomb D, et al. (2022). The whisking oscillator circuit. Nature 609, 560–568. 10.1038/S41586-022-05144-8. [PubMed: 36045290]

60. Moore JD, Deschênes M, Furuta T, Huber D, Smear MC, Demers M, and Kleinfeld D. (2013). Hierarchy of orofacial rhythms revealed through whisking and breathing. Nature 497, 205–210. 10.1038/NATURE12076. [PubMed: 23624373]

61. Yang CF, Kim EJ, Callaway EM, and Feldman JL (2020). Monosynaptic projections to excitatory and inhibitory pre-Bötzinger complex neurons. Front. Neuroanat. 14, 58. 10.3389/FNANA.2020.00058/BIBTEX. [PubMed: 33013329]

62. Guyenet PG, Stornetta RL, Souza GMPR, Abbott SBG, Shi Y, and Bayliss DA (2019). The retrotrapezoid nucleus: central chemoreceptor and regulator of breathing automaticity. Trends Neurosci. 42, 807–824. 10.1016/J.TINS.2019.09.002. [PubMed: 31635852]

63. Paton JFR, Abdala APL, Koizumi H, Smith JC, and St-John WM (2006). Respiratory rhythm generation during gasping depends on persistent sodium current. Nat. Neurosci. 9, 311–313. 10.1038/NN1650. [PubMed: 16474390]

64. Wei XP, Collie M, Dempsey B, Fortin G, and Yackle K (2022). A novel reticular node in the brainstem synchronizes neonatal mouse crying with breathing. Neuron 110, 644–657.e6. 10.1016/J.NEURON.2021.12.014. [PubMed: 34998469]

65. Rekling JC, Champagnat J, and Denavit-Saubié M (1996). Electroresponsive properties and membrane potential trajectories of three types of inspiratory neurons in the newborn mouse brain stem in vitro. J. Neurophysiol. 75, 795–810. 10.1152/JN.1996.75.2.795. [PubMed: 8714653]

66. Kallurkar PS, Grover C, Picardo MCD, and Del Negro CA (2020). Evaluating the burstlet theory of inspiratory rhythm and pattern generation. eNeuro 7, ENEURO.0314–19.2019. 10.1523/ENEURO.0314-19.2019.

67. Kam K, Worrell JW, Janczewski WA, Cui Y, and Feldman JL (2013). Distinct inspiratory rhythm and pattern generating mechanisms in the pre-Bötzinger Complex. J. Neurosci. 33, 9235–9245. 10.1523/JNEUROSCI.4143-12.2013. [PubMed: 23719793]

68. Ashhad S, and Feldman JL (2020). Emergent elements of inspiratory rhythmogenesis: network synchronization and synchrony propagation. Neuron 106, 482–497.e4. 10.1016/j.neuron.2020.02.005. [PubMed: 32130872]

69. Bankhead P, Loughrey MB, Fernández JA, Dombrowski Y, McArt DG, Dunne PD, McQuaid S, Gray RT, Murray LJ, Coleman HG, et al. (2017). QuPath: open source software for digital pathology image analysis. Sci. Rep. 7, 16878. 10.1038/s41598-017-17204-5. [PubMed: 29203879]

70. Schindelin J, Arganda-Carreras I, Frise E, Kaynig V, Longair M, Pietzsch T, Preibisch S, Rueden C, Saalfeld S, Schmid B, et al. (2012). Fiji - an open source platform for biological image analysis. Nat. Methods 9, 676–682. 10.1038/NMETH.2019. [PubMed: 22743772]

71. National Research Council (2011). Guide for the Care and Use of Laboratory Animals (National Academies Press). 10.17226/12910.

72. Percie du Sert N, Hurst V, Ahluwalia A, Alam S, Avey MT, Baker M, Browne WJ, Clark A, Cuthill IC, Dirnagl U, et al. (2020). The ARRIVE guidelines 2.0: updated guidelines for reporting animal research. Exp. Physiol. 105, 1459–1466. 10.1113/EP088870. [PubMed: 32666546]

73. Leary S, Underwood W, Anthony R, Cartner S, Grandin T, Greenacre C, Gwaltney-Brant S, McCrackin M, Meyer R, Miller D, et al. (2020). AVMA Guidelines for the Euthanasia of Animals: 2020 Edition (American Veterinary Medical Association (AVMA)).

74. Mortola JP, and Frappell PB (2013). Measurements of air ventilation in small vertebrates. Respir. Physiol. Neurobiol. 186, 197–205. 10.1016/j.resp.2013.02.001. [PubMed: 23419521]

75. Mortola JP, and Frappell PB (1998). On the barometric method for measurements of ventilation, and its use in small animals. Can. J. Physiol. Pharmacol. 76, 937–944. 10.1139/y99-001. [PubMed: 10100874]

76. Jacky JP (1978). A plethysmograph for long-term measurements of ventilation in unrestrained animals. J. Appl. Physiol. Respir. Environ. Exerc. Physiol. 45, 644–647. 10.1152/jappl.1978.45.4.644. [PubMed: 101497]

77. Drorbaugh JE, and Fenn WO (1955). A barometric method for measuring ventilation in newborn infants. Pediatrics 16, 81–87. [PubMed: 14394741]

78. Mortola JP (1984). Breathing pattern in newborns. J. Appl. Physiol. Respir. Environ. Exerc. Physiol. 56, 1533–1540. 10.1152/jappl.1984.56.6.1533. [PubMed: 6735812]

79. Cummings KJ, Hewitt JC, Li A, Daubenspeck JA, and Nattie EE (2011). Postnatal loss of brainstem serotonin neurons compromises the ability of neonatal rats to survive episodic severe hypoxia. J. Physiol. 589, 5247–5256. 10.1113/jphysiol.2011.214445. [PubMed: 21911619]

80. Koteja P (1996). Measuring energy metabolism with open-flow respiremetric systems: which design to choose? Funct. Ecol. 10, 675–677. 10.2307/2390179.

81. Chang K, Marran K, Valentine A, and Hannon GJ (2013). Creating an miR30-based shRNA vector. Cold Spring Harb. Protoc. 2013, 631–635. 10.1101/PDB.PROT075853. [PubMed: 23818675]

82. Dow LE, Premsrirut PK, Zuber J, Fellmann C, McJunkin K, Miething C, Park Y, Dickins RA, Hannon GJ, and Lowe SW (2012). A pipeline for the generation of shRNA transgenic mice. Nat. Protoc. 7, 374–393. 10.1038/NPROT.2011.446. [PubMed: 22301776]

83. Calin-Jageman RJ, and Cumming G (2019). Estimation for better inference in neuroscience. eNeuro 6, ENEURO.0205–19.2019. 10.1523/ENEURO.0205-19.2019.

Highlights

- Deleting *Scn8a* in core breathing neurons reduces I_{NaP}, prevents pacemaker bursting

- Conditional *Scn8a* knockout in core neurons affects breathing development

- Conditional *Scn8a* knockdown in core neurons does not affect adult breathing

- I_{NaP} and pacemaker activity influence core breathing neurons but are dispensable
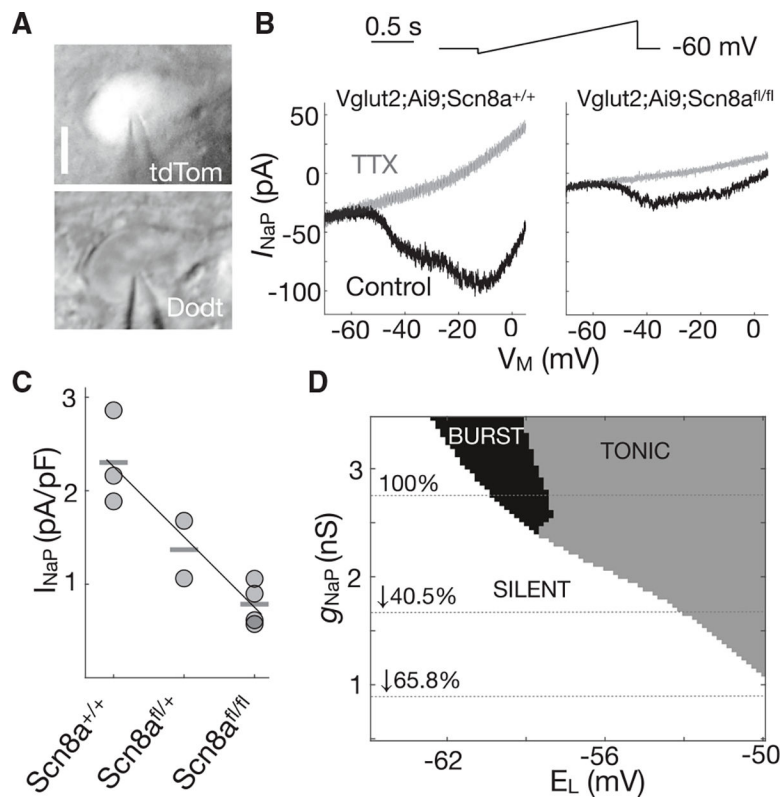
Figure 1. Conditional knockout of *Scn8a* reduces I_{NaP} in glutamatergic preBötC neurons

(A) *VGlut2*-expressing neurons in the preBötC identified via tdTomato (tdTom or Ai9) fluorescence (top) and with differential interference contrast imaging (dubbed "Dodt" by Zeiss, bottom) during patch-clamp recording. Calibration bar shows 10 μm.

(B) Voltage-ramp commands (top) applied during patch-clamp recordings and quasi-steady-state current-voltage (I-V) curves (bottom) from glutamatergic neurons in *VGlut2;Ai9;Scn8a^+/+* (left) and *VGlut2;Ai9;Scn8a^fl/fl* (right) mouse slices. Gray lines show I-V curves after TTX application.

(C) Plot of peak I_{NaP} vs. mouse genotype: *VGlut2;Ai9;Scn8a^+/+*, *VGlut2;Ai9;Scn8a^fl/+*, and *VGlut2;Ai9;Scn8a^fl/fl*. Gray circles show individual neuron; horizontal gray line shows the mean for each group. Genotype labels are shortened for display convenience.

(D) Behavior of a mathematical model of a canonical preBötC bursting-pacemaker neuron for different values of persistent Na$^+$ conductance (g_{NaP}) and the reversal potential of a K$^+$-dominated leakage current (E_L). Three activity states are shown according to the ratio between g_{NaP} and E_L: silent, bursting, and tonically spiking. Horizontal dotted lines show the behaviors supported by the model when g_{NaP} is decreased from its standard value.
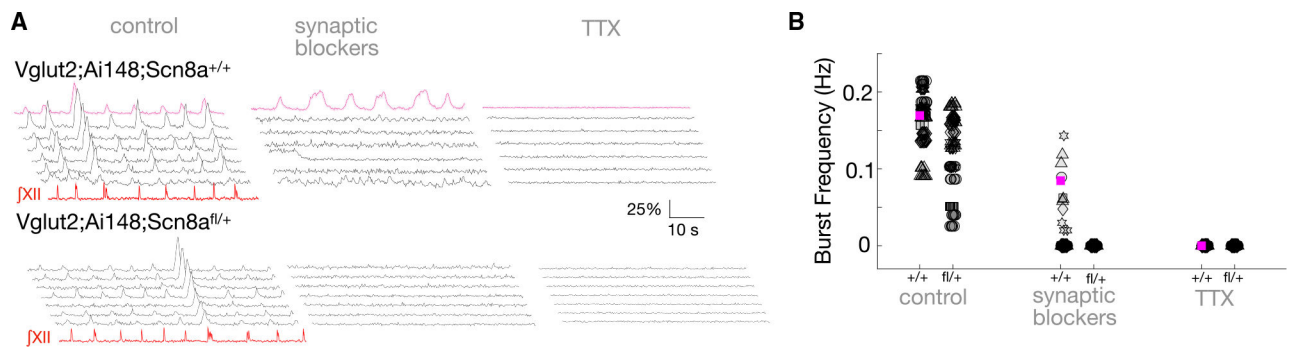
Figure 2. Conditional knockout of *Scn8a* in glutamatergic neurons precludes pacemaker activity and slows but does not stop inspiratory rhythm

(A) Calcium activity in glutamatergic preBötC neurons from *VGlut2;Ai148;Scn8a*$^{+/+}$ (wild type, top panels) and *VGlut2;Ai148;Scn8a*$^{fl/+}$ (heterozygous, bottom panels) mouse slices. Multiphoton imaging traces are displayed with the inspiratory motor output from the XII cranial nerve (red). Each black trace represents one preBötC neuron, and the magenta trace refers to a single neuron also shown in magenta in (B). Neuronal activity was recorded under three different conditions: control (left) with standard artificial cerebrospinal fluid (ACSF) bathing solution, ionotropic synaptic receptor blockers (middle), and TTX (right).

(B) Burst frequency of neurons from *VGlut2;Ai148;Scn8a*$^{+/+}$ (+/+) and *VGlut2;Ai148;Scn8a*$^{fl/+}$ (fl/+) mouse slices. Translucent gray symbols represent single neurons; all neurons from the same slice were assigned the same symbol. As in (A), from left to right, neuronal activity was recorded under three different conditions: control, ionotropic synaptic receptor blockers, and TTX. The control condition reflects collective activity of all neurons in sync in a rhythmic slice. The synaptic blockers condition shows the subset of neurons with bursting-pacemaker activity after synaptic isolation, but most of the neurons remain quiescent. In TTX, all neurons were quiescent.
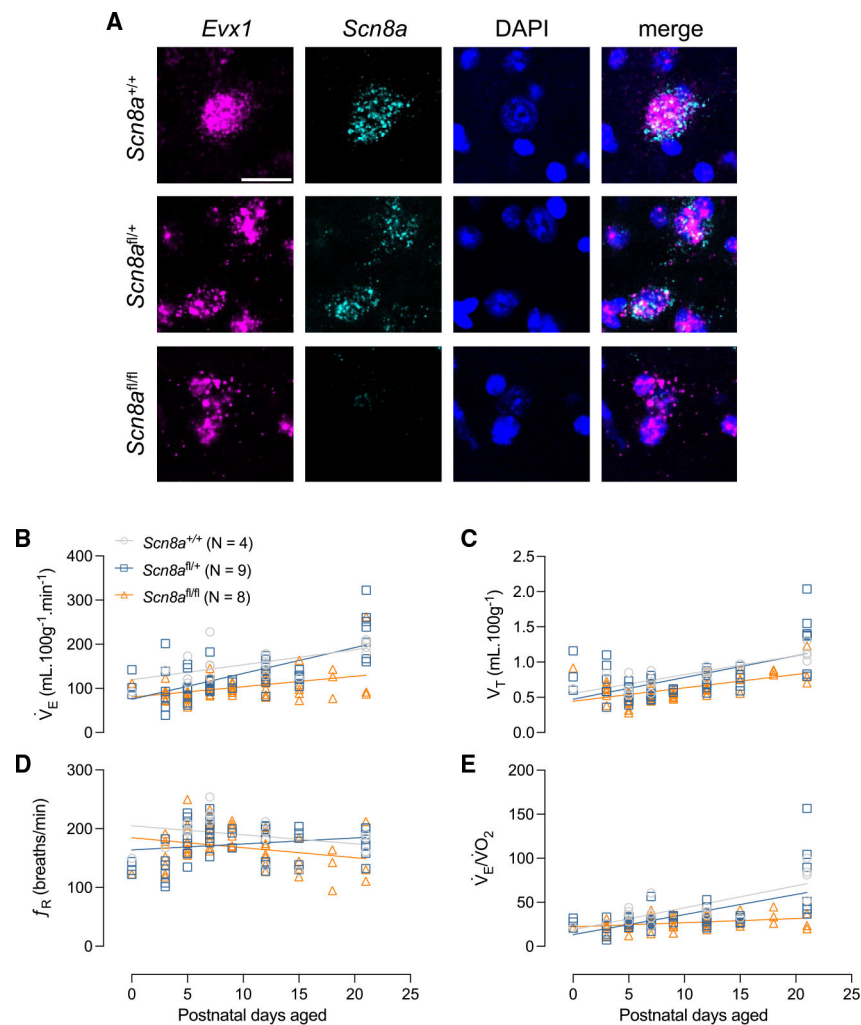
Figure 3. *Scn8a* **expression and ventilation are diminished in Dbx1;Scn8a conditional knockout mice during postnatal development**

(A) RNAscope images showing transcripts of *Evx1* (magenta) and *Scn8a* (cyan). DAPI (blue) shows nuclear staining. The images were merged for co-localization. Sections from *Dbx1;Scn8a^{+/+}*, *Dbx1;Scn8a^{fl/+}*, and *Dbx1;Scn8a^{fl/fl}* mice organized by row. Genotype labels are shortened for display convenience. Calibration bar shows 20 μm. See also Figures S1 and S2.

(B–E) Respiratory variables of *Dbx1;Scn8a^{+/+}* (gray, N = 4), *Dbx1;Scn8a^{fl/+}* (blue, N = 9), and *Dbx1;Scn8a^{fl/fl}* (orange, N = 8) mice, measured from P0–P21: ventilation $\left(\dot{V}_E\right)$ in (B), tidal volume (V_T) in (C), breathing frequency (f_R) in (D), and the air convection requirement $\left(\dot{V}_E/\dot{V}_{O_2}\right)$ in (E). Genotype labels are shortened for display convenience. Open symbol represents individual animals, and continuous lines represent linear regression analyses for each group. See also Figures S3 and S4.
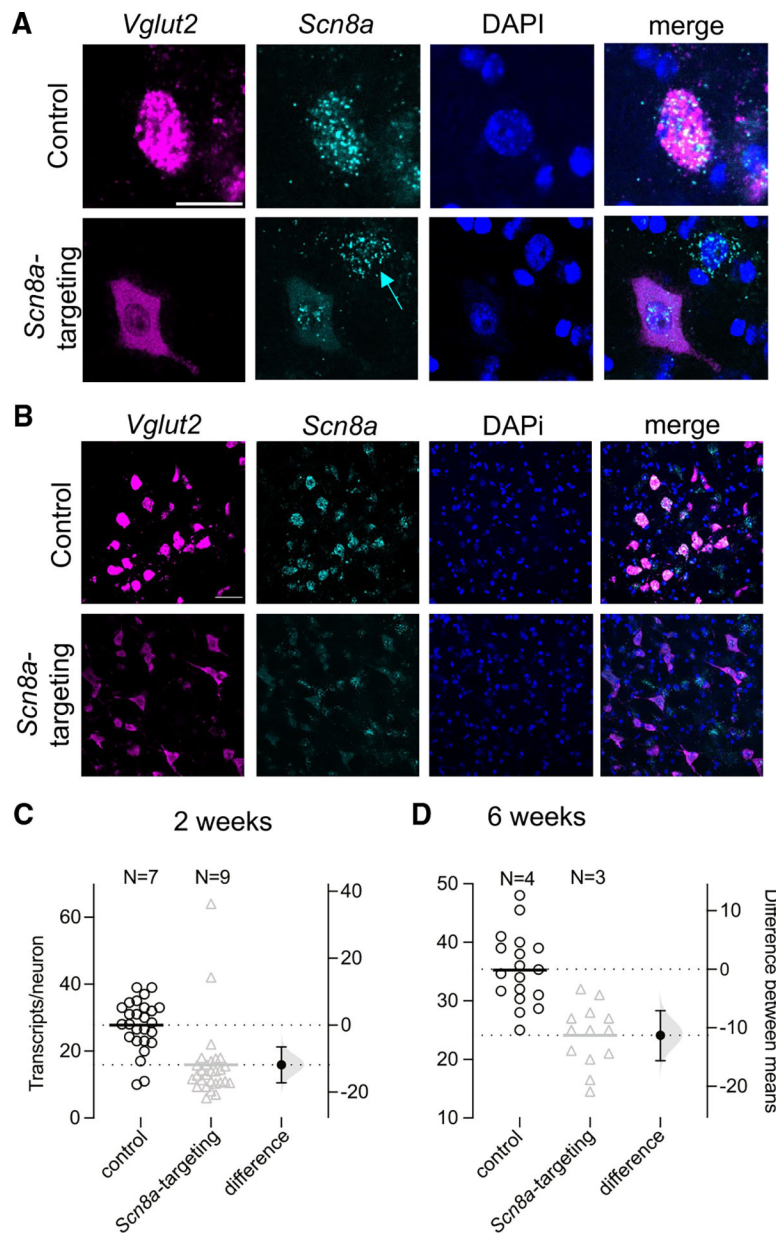
Figure 4. *Scn8a*-targeting shRNA decreases gene expression

(A and B) Coronal sections of RNAscope performed in VGlut2-ires-cre mice injected with non-targeting shRNA sequence (control) or *Scn8a*-targeting shRNA sequence.

(A) mCherry-positive glutamatergic (*VGlut2*) neurons (magenta). Other columns show *Scn8a* (cyan), DAPI-stained nuclei (blue), and the merge of the three previous images, respectively. The cyan arrow on the second picture of the *Scn8a*-targeting group indicates abundant *Scn8a* transcripts in a neuron not transduced with AAV9. Calibration bar shows 20 μm.

(B) Lower-magnification images organized as in (A). Calibration bar shows 50 μm. See also Figures S6 and S7.

(C and D) Dot-scatter plots with effect size (i.e., estimation statistics showing the difference in means with 95% confidence intervals). The number of the *Scn8a* transcripts per *VGlut2*-

expressing preBötC neuron in sections from control mice (black circles) and in mice injected with *Scn8a*-targeting shRNA (gray triangles) at 2 (C) and 6 weeks (D) after AAV9 injection. Symbols represent single sections; horizontal lines represent means. Black filled circle shows the difference in the means with 95% confidence intervals and a superimposed normal distribution reflecting these data (gray).
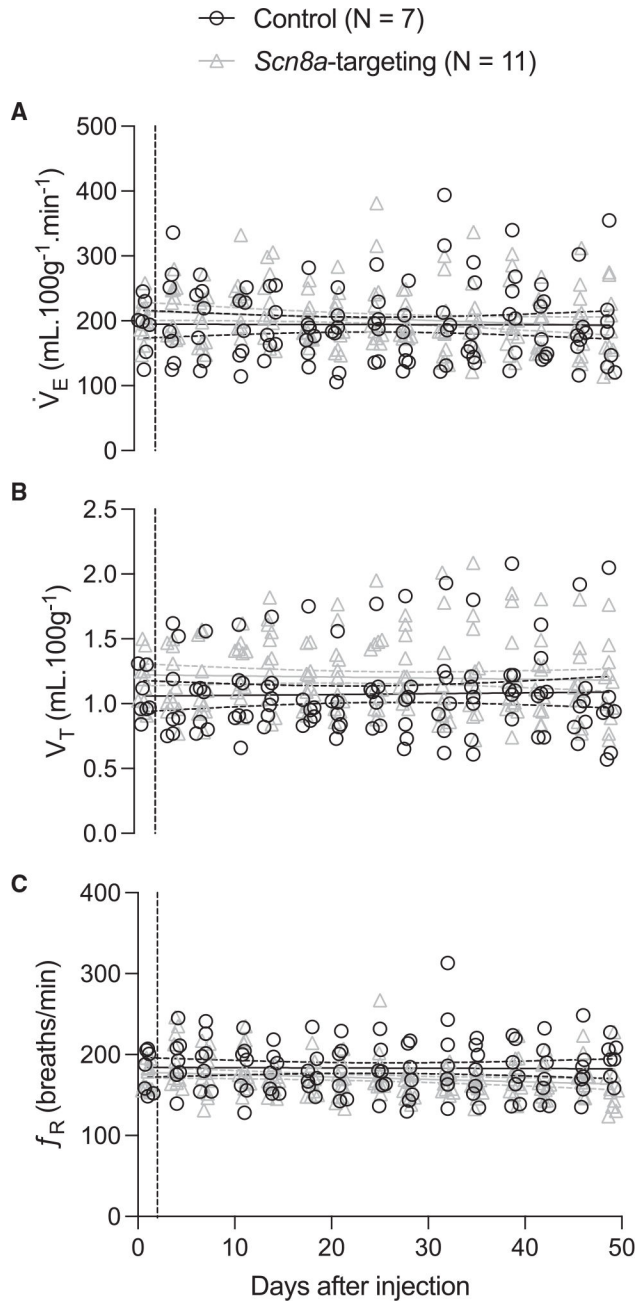
Figure 5. shRNA injection in the preBötC does not affect the respiratory variables in unanesthetized adult VGlut2-ires-cre mice

Respiratory variables of mice injected with a non-targeting (control, black circles, N = 7) or *Scn8a*-targeting (gray open triangles, N = 11) shRNA sequence, measured for 49 days after the injection: $\dot{V}_E$ in (A), V_T in (B), and f_R in (C). Vertical dashed lines indicate the day of the injection. Individual symbols represent measurements from single mice. Horizontal continuous lines show linear regression; dashed lines show the 95% confidence intervals for the regression lines. See also Figures S8, S9 and S10.

Table 1.

Linear regression of the ventilation ($\dot{V}_E$), tidal volume (V_T), respiratory frequency (f_R), air convection requirement ($\dot{V}_E/\dot{V}_{O_2}$), oxygen consumption ($\dot{V}_{O_2}$), inspiratory time (T_I), expiratory time (T_E), and inspiratory drive (V_T/T_I) of wild-type ($Dbx1;Scn8a^{+/+}$), heterozygous ($Dbxi;Scn8a^{fl/+}$), and homozygous ($Dbx1;Scn8a^{fl/fl}$) mice

	$Dbx1;Scn8a^{+/+}$ (N = 4)			$Dbx1;Scn8a^{fl/+}$ (N = 9)			$Dbx1;Scn8a^{fl/fl}$ (N = 8)		
	m	r^2	p	m	r^2	p	m	r^2	p
$\dot{V}_E$	3.41	0.38	4.85×10^{-3a}	5.86	0.45	7.74×10^{-8a}	2.37	0.16	3.59×10^{-3a}
V_T	0.03	0.71	6.53×10^{-6a}	0.03	0.35	5.43×10^{-6a}	0.02	0.34	8.47×10^{-6a}
f_R	−1.53	0.10	0.19	1.02	0.04	0.18	−1.69	0.07	0.06
$\dot{V}_E/\dot{V}_{O_2}$	2.49	0.58	1.39×10^{-4a}	2.28	0.35	5.20×10^{-6a}	0.47	0.13	0.01^a
$\dot{V}_{O_2}$	−0.09	0.44	1.90×10^{-3a}	−0.03	0.02	0.29	−0.01	0.002	0.75
T_I	3.94×10^{-3}	0.48	0.13	-2.66×10^{-3}	0.08	0.09	1.21×10^{-4}	2.19×10^{-4}	0.92
T_E	-1.13×10^{-3}	0.02	0.79	-7.11×10^{-3}	0.29	8.00×10^{-4a}	3.51×10^{-3}	0.08	0.04^a
V_T/T_I	0.06	0.11	0.51	0.23	0.54	4.70×10^{-7a}	0.11	0.13	0.01^a

Measurements were performed from postnatal day 0(P0) up to P27–P28. $\dot{V}_E$ is in units of mL min^{-1} 100 g^{-1}. V_T is in units of mL min^{-1} 100 g^{-1}. f_R is in units of breaths min^{-1}. $\dot{V}_E/\dot{V}_{O_2}$ is unitless. $\dot{V}_{O_2}$ is in units of mL min^{-1} 100 g^{-1}. T_I and T_E are in units of s. V_T/T_I is in units of mL s^{-1} 100 g^{-1}. All slopes (m) are calculated per day of observation, i.e., unit d^{-1}. r^2, coefficient of determination. See also Figure S4.

^{a}The slope "m" significantly deviates from zero.

Table 2.

Linear regression of the ventilation ($\dot{V}_E$), tidal volume (V_T), respiratory frequency (f_R), air convection requirement ($\dot{V}_E/\dot{V}_{O_2}$), inspiratory time (T_I), expiratory time (T_E), and inspiratory drive (V_T/T_I) of adult mice injected with AAVs carrying non-targeting (control) and *Scn8a*-targeting shRNA in the preBötC

	Control (N = 7)			Scn8a targeting (N = 11)		
	m	r²	P	m	r²	P
$\dot{V}_E$	−0.02	3.33×10^{-5}	0.95	−0.47	0.02	0.06
V_T	6.36×10^{-4}	8.50×10^{-4}	0.77	-8.44×10^{-4}	0.002	0.58
f_R	−0.03	2.47×10^{-4}	0.87	−0.30	0.04	0.02^a
T_I	-4.08×10^{-3}	0.11	0.0007^a	1.70×10^{-3}	0.005	0.37
T_E	7.67×10^{-4}	0.04	0.04^a	4.09×10^{-4}	0.02	0.09
V_T/T_I	0.05	0.03	0.06	-5.57×10^{-4}	6.02×10^{-6}	0.98

$\dot{V}_E$ is in units of mL min^{-1} 100 g^{-1}. V_T is in units of mL 100 g^{-1}. f_R is in units of breaths min^{-1}. T_I and T_E are in units of s. V_T/T_I is in units of mLs^{-1} 100 g^{-1}. All slopes (m) are calculated per day of observation, i.e., unit d^{-1}. r^2, coefficient of determination. See also Figure S9.

^{a}The slope "m" significantly deviates from zero.

KEY RESOURCES TABLE

REAGENT or RESOURCE	SOURCE	IDENTIFIER
Bacterial and virus strains		
Scn8a-targeting shRNA: Ultra-purified custom miR30-based shRNA AAV9 virus	VectorBuilder	Cat# MixAAV9SP(1395 + 1396+1397)
Control shRNA: Ultra-purified custom gene expression scAAV9 virus	VectorBuilder	Cat# AAV9SP(VB190930-1224ajh)
Biological samples		
Ear punch	This paper	N/A
Tail snip	This paper	N/A
Brain slices	This paper	N/A
Chemicals, peptides, and recombinant proteins		
Opal 520 Reagent Pack	Akoya Biosciences	Cat# FP1487001KT
Opal 690 Reagent Pack	Akoya Biosciences	Cat# FP1497001KT
Invitrogen™ ProLong™ Gold Antifade Mountant	FisherScientific	Cat# P36934
RNAscope 3-plex negative control probes	Advanced Cell Diagnostics, Inc.	Cat# 320871
RNAscope Probe Diluent	Advanced Cell Diagnostics, Inc.	Cat# 300041
NaCl	FisherScientific	Cat# S25542A
KCl	FisherScientific	Cat# P217-500
$CaCl_2$	FisherScientific	BP510-250
$MgSO_4$	FisherScientific	M65-500
$NaHCO_3$	FisherScientific	Cat# S25533A
NaH_2PO_4	FisherScientific	Cat# S369-500
dextrose	FisherScientific	N/A
tetraethylammonium-chloride	Sigma	T2265-100G
EGTA	Sigma	324626-25GM
HEPES	FisherScientific	Cat# BP310-100
CsCl	FisherScientific	Cat# 206320250
Isoflurane Solution	Covetrus	Cat# 11695067772
Phosphate-buffered saline 10X	FisherScientific	Cat# BP665-1
Paraformaldehyde	Sigma-Aldrich	Cat# 158127-500G
Tris-buffered saline solution with Tween 20X	Thermo Scientific	Cat# J77500-K2
Critical commercial assays		
RNAscope Multiplex Fluorescent Reagent Kit v2	Advanced Cell Diagnostics, Inc.	Cat# 323100
Experimental models: Organisms/strains		
Mouse: VGlut2-ires-cre (*Slc17a6tm2(cre>Lowl)*)	The Jackson Laboratory	RRID:IMSR_JAX:016963

REAGENT or RESOURCE	SOURCE	IDENTIFIER
Mouse: Ai9 (B6; 129S6-*Gt(ROSA)26Sor*$^{tm9(CAG-tdTomato)Hze}$/**J**)	The Jackson Laboratory	RRID:IMSR_JAX:007905
Mouse: Ai148 (B6.Cg-*Igs7*$^{tm148-1(tetO-GCaMP6f,CAG-tTA2)Hze}$/**J**	The Jackson Laboratory	RRID:IMSR_JAX:030328
Oligonucleotides		
RNAscope™ Probe- Mm-Scn8a	Advanced Cell Diagnostics, Inc.	Cat# 434191
RNAscope™ Probe- Mm-Evx1-C3	Advanced Cell Diagnostics, Inc.	Cat# 509161-C3
RNAscope™ Probe- mCherry-C3	Advanced Cell Diagnostics, Inc.	Cat# 431201-C3
Scn8a PCR Primer	Integrated DNA Technologies	Custom made
Dbx1^{Cre} PCR Primer	Integrated DNA Technologies	Custom made
VGlut2^{Cre} PCR Primer	Integrated DNA Technologies	Custom made
Software and algorithms		
GraphPad Prism v9.5.1	GraphPad	RRID:SCR_002798
QuPath v0.3.2	Bankhead et al.[69]	RRID:SCR_018257
Fiji - ImageJ2 v.2.9.0/1.53t	Schneider et al.[70]	RRID:SCR_002285
LabChart Pro v.8.1.17	ADInstruments	RRID:SCR_023643
ThorImage LS v.4.1	ThorLabs	https://www.thorlabs.com/newgrouppage9.cfm?objectgroup_id=9072#ad-image-0
MATLAB v.2021a	MathWorks	RRID:SCR_001622
PATCHMASTER	HEKA Electronic	RRID:SCR_000034